CELL BIOLOGY

Three-dimensional cell-cell interactions promote direct reprogramming of patient fibroblasts into functional and transplantable neurons

Janko Kajtez[1]*†, Kerstin Laurin[1]†, Fredrik Nilsson[1], Andreas Bruzelius[1], Efrain Cepeda-Prado[1], Marcella Birtele[1], Roger A. Barker[2], Freja Herborg[3], Daniella Rylander Ottosson[1], Petter Storm[1], Alessandro Fiorenzano[1,4], Mette Habekost[1,5], Malin Parmar[1]*

Direct reprogramming of somatic cells into induced neurons (iNs) has become an attractive strategy for the generation of patient-specific neurons for disease modeling and regenerative neuroscience. To this end, adult human dermal fibroblasts (hDFs) present one of the most relevant cell sources. However, iNs generated from adult hDFs using two-dimensional cultures are difficult to maintain in vitro and face challenges in survival upon transplantation into the adult brain, thus imposing constraints on biomedical applications of iN technology. Here, we present a platform for direct in vitro reprogramming of adult hDFs inside three-dimensional suspension microcultures (3D-iNs). We show that the 3D environment favors neuronal over fibroblast cellular identity to yield more robust conversion into functional neurons with extended culturing span. The 3D reprogramming approach also provides a platform for fusion into induced assembloids. 3D-iNs can be gently harvested and transplanted into the adult rodent brain to reproducibly generate neuron-rich grafts, thus eliminating a major bottleneck in the direct reprogramming field.

INTRODUCTION

Recent breakthroughs in cellular reprogramming have paved the way for direct cell-fate conversion of somatic cells such as fibroblasts into induced neurons (iNs) without transitioning through an intermediate proliferative state (*1*–*3*). Direct reprogramming can successfully yield specific neuronal subtypes using defined sets of transcription factors and fate determinants [e.g., dopaminergic (DA) (*4*, *5*), cholinergic (*6*), striatal medium spiny (*7*), and GABAergic (*8*, *9*)]. As such, this challenges the traditional views on cell identity and opens new opportunities in biomedical research and clinical applications (*10*). Besides being an invaluable tool to create patient and disease-specific neurons for modeling of age-associated neurological disorders (*11*–*15*), direct reprogramming offers a promising nonpluripotent cell source for personalized transplantation-based therapies for neurodegenerative diseases. Adult human dermal fibroblasts (hDFs) stand out as the most relevant patient-derived cell source for these applications while also being one of the most challenging somatic cell types to convert into neuronal cells (*4*, *16*, *17*). In addition, iNs generated from adult hDFs in two-dimensional (2D) cultures show suboptimal long-term viability in vitro. Moreover, although transplantation of directly converted neurons have been investigated in a few transplantation studies, survival and integration of the transplanted neurons has only been achieved using murine fibroblasts (*8*) or human embryonic fibroblasts (*18*) or when adult hDF-derived iNs were transplanted into the more supportive early postnatal mouse brain (*19*, *20*). Therefore, survival after intracerebral grafting and functional integration of patient-derived iNs into the adult brain remain a critical, unresolved challenge, representing a major barrier that must be overcome before their potential in cell replacement therapy or in vivo disease modeling can be explored.

An inherent shortcoming of 2D cultures is the need to enzymatically or mechanically dissociate cells from the substrate before harvesting and transplantation, resulting in substantial cell death. 3D culturing methodology has the potential to overcome this issue (*21*). Yet, direct reprogramming of fibroblasts in 3D remains largely unexplored, with only a recent proof-of principle study using mouse embryonic fibroblasts and a bulk hydrogel culture approach that still required sample dissociation and offered limited translational potential (*22*). We hypothesized that sufficiently small self-supported 3D cellular structures could provide a beneficial environment permissive to direct cell-fate conversion while allowing long-term culturing and being both readily injectable (without the need for cell dissociation) and protective against mechanical and biological stresses during the transplantation procedure. To test the hypothesis, we developed a strategy for direct in vitro reprogramming of adult hDFs inside suspension 3D microculture arrays (Fig. 1A). This approach relies on the ability of fibroblasts to self-assemble into compact spherical structures when devoid of substrate-interactive features. In parallel to cellular self-assembly taking place, lentivirus-mediated expression of a defined set of transcription factors initiates cell-fate conversion of hDFs into iNs. Using this approach, we were able to create thousands of induced neurospheroids, here termed 3D-iNs. Notably, the 3D platform provides environmental selection that favors neuronal over fibroblast cell identity. An additional benefit of 3D reprogramming is that it allows fusion of independently reprogrammed neuronal cultures. We further demonstrate that the 3D reprogramming platform supports the generation of subtype-specific

[1]Department of Experimental Medical Sciences, Wallenberg Neuroscience Center, Division of Neurobiology and Lund Stem Cell Center, BMC A11, Lund University, S-22184 Lund, Sweden. [2]John van Geest Centre for Brain Repair & Department of Neurology, Department of Clinical Neurosciences and Wellcome-MRC Cambridge Stem Cell Institute, University of Cambridge, Cambridge, UK. [3]Department of Neuroscience, Faculty of Health and Medical Sciences, University of Copenhagen, Copenhagen, Denmark. [4]Department of Molecular Medicine and Medical Biotechnology, University of Naples Federico II, Naples, Italy. [5]Center for Translational Neuromedicine, University of Copenhagen Faculty of Health and Medical Sciences, 2200 Copenhagen N, Denmark.
*Corresponding author. Email: malin.parmar@med.lu.se (M.P.); janko.kajtez@med.lu.se (J.K.)
†These authors contributed equally to this work.

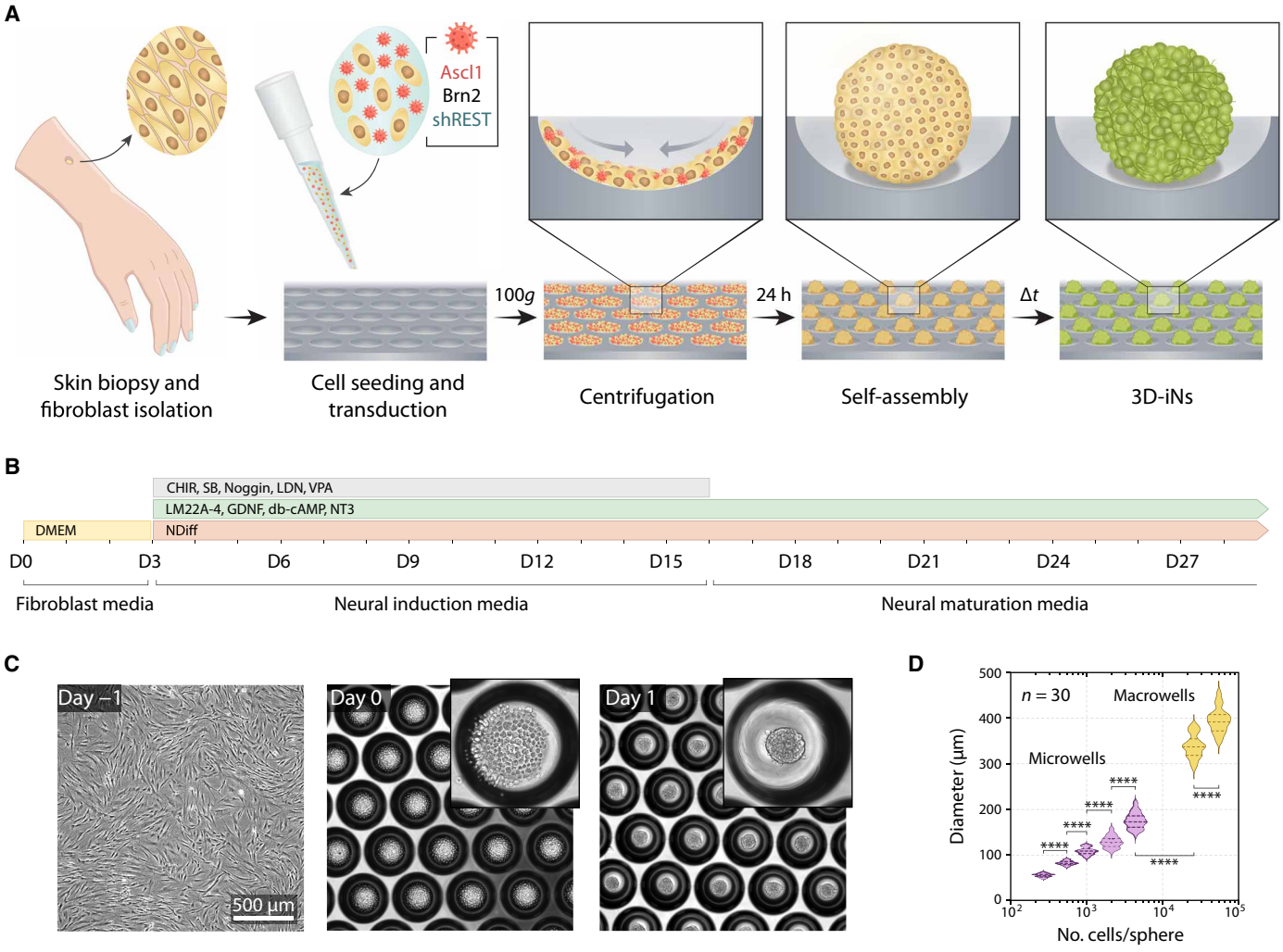

Fig. 1. Methodology of 3D-iN generation. (**A**) Schematic illustration depicting major steps in the developed procedure for direct reprogramming of hDFs in suspension 3D microcultures to generate arrays of 3D-iNs. h, hours. (**B**) Reprogramming timeline showing media composition used at different stages of the protocol. (**C**) Bright-field images showing reproducible self-assembly of hDFs into spheres within 24 hours after seeding into arrays of ultralow attachment conical microwells. (**D**) Measurements of sphere diameter 48 hours after cell seeding demonstrate the ability to reproducibly tune the size of 3D-iNs according to the number of cells seeded in each well. ****$P < 0.0001$, unpaired *t* test between consecutive conditions.

neurons, as evidenced by the formation of induced DA neurospheroids (3D-iDANs) when DAergic fate determinants are added to the reprogramming cocktail. 3D-iDANs can be gently harvested without the need for enzymatic or mechanical dissociation and are compatible with the glass capillaries routinely used in the preclinical setting for precise intracerebral injection of cell suspensions (*23*). We demonstrate that, in contrast to cells reprogrammed in conventional 2D culture, iNs reprogrammed in 3D survive transplantation into the adult rodent brain and reproducibly generate healthy neuron-rich grafts. The grafted cells survive long-term with evidence of electrophysiological maturation and functional integration into the host circuitry.

RESULTS

Direct neuronal reprogramming of adult hDFs inside 3D microcultures

The suspension 3D reprogramming approach presented here was designed to be compatible with long-term in vitro culture as well as with standard procedures for intracerebral cell transplantation. As such, it needed to fulfill several requirements: (i) reproducibly create spheroids of a given size, (ii) ensure an even distribution of lentivirally delivered conversion factors, (iii) maintain spatial separation of individual spheroids during the culturing period without the risk of fusion to form bigger aggregates, (iv) enable gentle harvesting of spheroids for transplantation without the need for cellular dissociation, and (v) easy scale-up to allow for high-throughput production able to accommodate larger studies. To achieve this, we seeded adult hDFs on an array of conical microwells with ultralow attachment surface. Lentivirus was mixed with cells during seeding to ensure homogeneous exposure (Fig. 1A). After gentle centrifugation, we observed that cells were distributed evenly between microwells in the array. Within 24 hours, hDFs in each microwell self-assembled into well-defined spherical structures (Fig. 1C). The presence of clear edges to these structures and the lack of wells with individual nonintegrated cells indicated that there was a high efficacy to the aggregation process.

We successfully generated hDF spheres with defined sizes ranging from 68 ± 5 to 179 ± 18 μm in diameter corresponding to 250 and 4000 cells per sphere in each microwell, respectively (Fig. 1D). Seeding less than 250 cells in each microwell resulted in inconsistent aggregate formation with compromised structure, indicating that a certain number of cells is required for successful and reproducible self-assembly. Conical macrowells were required when seeding more than 4000 cells for the generation of larger microspheres (e.g., 345 ± 26 μm in diameter for 30,000 cells per sphere).

The reprogramming was induced via expression of an all-in-one vector containing reprogramming factors *Ascl1* and *Brn2* accompanied by the knockdown of REST complex, a combination we previously identified as an efficient strategy for generating a high yield of iNs from adult hDFs across a diverse range of genetic backgrounds and ages in 2D cultures (*20*, *24*). For the first 2 weeks, spheres were cultured in neuronal induction medium containing selected small molecules and growth factors known to promote neuronal conversion. Afterward, maturation media that contained only the growth factors was used until the desired experimental endpoint (Fig. 1B).

The 3D-iN array remained spatially unperturbed during the culturing time with no evidence of fusion of adjacent microspheres (Fig. 2A). The day after seeding, microspheres were positive for the fibroblast marker vimentin but not for neuronal markers (Fig. 2B, top). By contrast, at day 30, we observed that 3D-iNs were positive for neuronal markers (MAP2 and TAU), confirming the change to neuronal identity (Fig. 2B, bottom). Quantification (n = 5894 cells) revealed the efficacy of conversion into $MAP2^+$ cells to be 49.5 ± 13.4, 39.8 ± 9.4, and 36.2 ± 8.1% for adult hDF lines #1, #2, and #3, respectively. Further characterization revealed that the population mostly consists of GABAergic neurons (GAD65/67) with a proportion expressing calbindin and calretinin, whereas DA (TH), glutamatergic marker (vGlut), and glial markers (GFAP and PDGFRA) were not detected (fig. S1). Next, we performed transcriptome-wide expression profiling of the 3D-iN reprogramming process. We took advantage of bulk RNA sequencing (RNA-seq) and compared the gene expression profiles between the starting hDFs and 3D-iNs at three different stages of reprogramming (days 2, 7, and 21). Principal components analysis (PCA) showed clear transcriptional differences between hDFs and cells undergoing 3D reprogramming (Fig. 2C). Analysis of 13 representative fibroblast-associated genes and 50 neuronal genes further verified successful neuronal reprogramming (Fig. 2D).

It is now well established that aging markers persist throughout direct fibroblast-to-neuron reprogramming in 2D (*12*, *14*). Here, we investigated whether the same is observed in 3D neuronal reprogramming. Using Horvath's clock (*25*) to analyze 353 epigenetic marks, we found no major changes in estimated age between 2D and 3D reprogrammed neurons (from three adult hDF lines) at the epigenetic level (Fig. 2E). On the other hand, as a control, resetting of the epigenetic clock was confirmed in induced pluripotent stem cells (iPSCs) generated from the same hDF lines (Fig. 2E).

It has been suggested that a spatially confined 3D environment could lead to partial mechanical reprogramming of fibroblasts toward a stem-like state (*26*). To investigate whether a self-assembled 3D environment could have an effect on the epigenetic age, we preconditioned hDFs in 3D microcultures for 3 or 6 days prior to the onset of reprogramming. However, no changes in epigenetic age were observed (Fig. 2E). On the contrary, we observed that 3D hDF microcultures (in fibroblast media, without neuronal conversion factors) deteriorated over time with visible debris accumulation (Fig. 2F) and shrinkage of microspheres (~8 times in volume; Fig. 2G). hDF cell death in 3D was further confirmed by live-dead staining whereas the same cell lines remained viable and proliferated as expected in conventional 2D culture (Fig. 2H). Reverse transcription quantitative polymerase chain reaction (RT-qPCR) analysis indicated an increase in apoptosis (*CASP3*) and decrease in proliferation (*MKI67*) when fibroblasts are cultured in 3D (Fig. 2I). Reduced proliferation was further confirmed at the protein level via immunocytochemistry (Fig. 2J). These results demonstrate that self-supported suspension microculture does not provide favorable conditions for fibroblast survival, suggesting that the 3D platform creates an environmental bias favoring the neuronal fate.

3D environment supports generation of subtype-specific neurons

Driving neuronal reprogramming toward specific neuronal subtypes is of great interest to both disease modeling and regenerative medicine. Given the growing interest in DA neurons for these purposes, we aimed to test whether direct neuronal 3D reprogramming can enhance also the reprogramming into functional and subtype-specific DA neurons. To test this, reprogramming was initiated via a reprogramming cocktail previously identified to give rise to DA neurons in 2D cultures: expression of six reprogramming factors (*Ascl1*, *Lmx1a, Lmx1b*, *FoxA2*, *Otx2,* and *Nurr1*) delivered through six individual lentiviral vectors and REST complex knockdown through two separate lentiviral vectors (Fig. 3A) (*14*).

Progressive maturation of the reprogrammed cells was investigated by RT-qPCR analysis, which demonstrated a time-dependent increase in the expression level of mature neuronal markers (*SYN*) and markers associated with DA neurons (*DAT*, *TH*, *AADC*, and *PITX3*) (Fig. 3B). Immunocytochemistry further confirmed successful reprogramming of hDFs into neurons (MAP2 and TUBB3) with the presence of DA neurons marked by tyrosine hydroxylase (TH; rate-limiting enzyme that catalyzes synthesis of DA precursor L-dopa) (Fig. 3C). Quantification revealed 53.4 ± 13.7% $MAP2^+$ cells of which 10.8 ± 4.2% expressed TH (Fig. 3D). Further immunofluorescence analysis revealed a proportion of TH^+ cells (n = 1167, three to four independent batches) to be also positive for ventral midbrain DA markers such as ALDH1A1 (27.6 ± 6.7%), GIRK2 (72.1 ± 18%), calbindin (20.7 ± 8.4%), VMAT2 (18.3 ± 8.4%), DAT (6.3 ± 3%), and DDC (11.4 ± 3.4%) (fig. S2A). Next, we compared the conversion efficacy between small (2000 cells per microsphere, ~120 μm in diameter) and large (30,000 cells per microsphere, ~350 μm in diameter) 3D-iDANs to test whether spheroids size affected neuronal conversion. We found no significant differences, indicating the size-independent reprogramming process (Fig. 3E). Neuronal maturation was also validated at the protein level with NeuN observed at day 50 (fig. S2B). To demonstrate that the reprogrammed neurons can be maintained in the 3D culture for longer periods, we kept 3D-iDANs in culture for 4 months (fig. S2C).

Next, we performed bulk RNA-seq and compared the gene expression profiles between hDFs and 3D-iDANs at three different stages of reprogramming (days 7, 30, and 50). PCA showed clear transcriptional differences between hDFs, cells in the intermediate reprogramming state (day 7), reprogrammed 3D-iDANs (days 30 and 50), and iDANs reprogrammed in 2D (Fig. 3F) with most of the variance explained by the time in vitro (first principal component). The difference was least pronounced between day 30 and 50 samples. Differential expression analysis of day 30 3D-iDANs

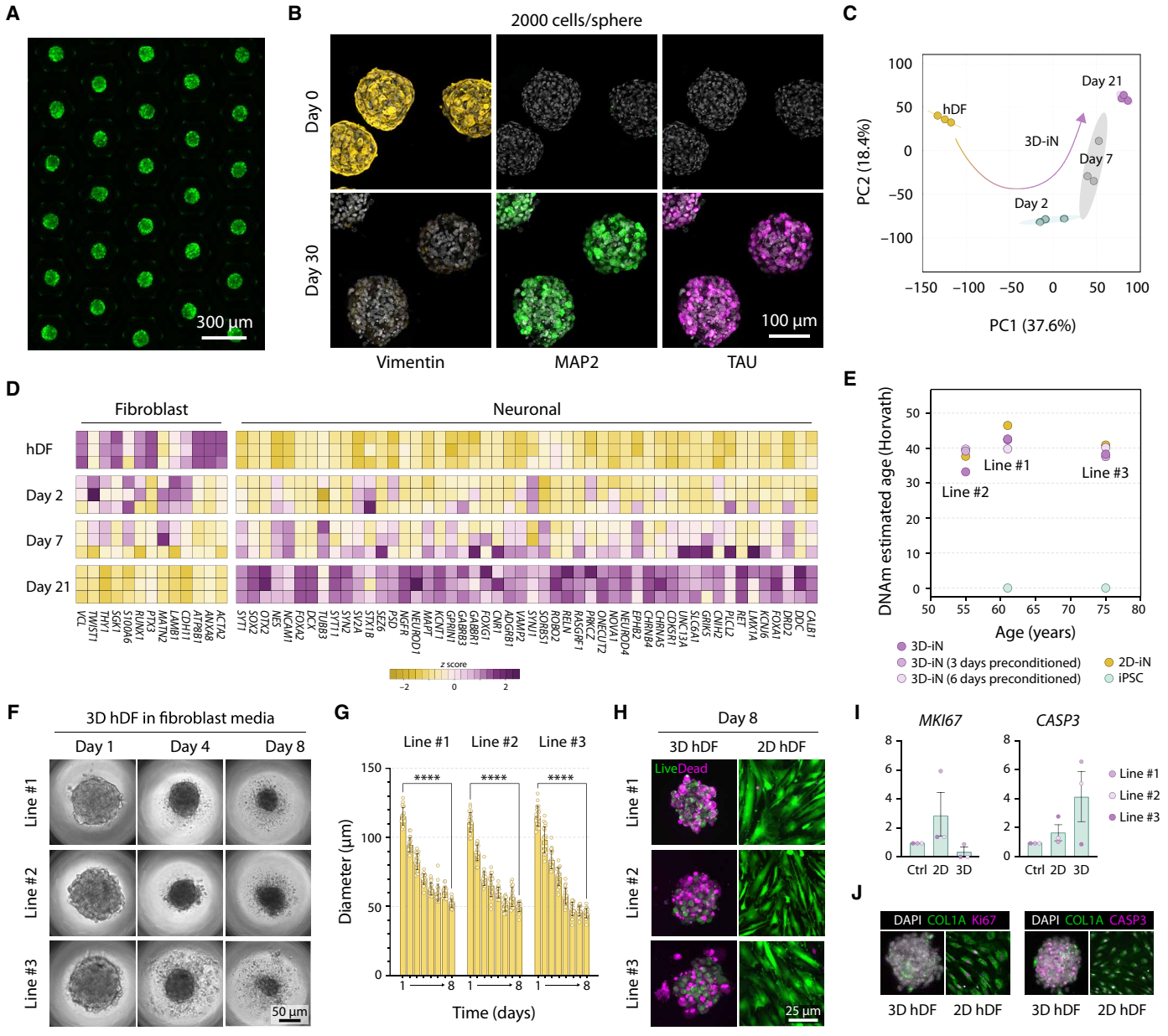

Fig. 2. Direct neuronal 3D reprogramming. (**A**) Fluorescence live-cell image showing a segment of a larger microculture array at day 30. Cells were labeled with PGK-GFP lentivirus. (**B**) Immunocytochemistry of cellular microspheres at day 1 and day 30 after the onset of reprogramming. Maximum intensity projections of fluorescence confocal image stack. (**C**) PCA of transcriptomic profiles obtained from hDFs, 3D-iNs at 2, 7, and 21 days. (**D**) Heatmap representation of expression levels of selected group of fibroblast and neuronal genes. Values log transformed and scaled by the mean expression of each gene across samples. (**E**) Epigenetic age as predicted by DNA methylation profiling of 3D-iNs, 2D-iNs, and iPSCs derived from hDF lines from three individuals. Preconditioning refers to maintaining hDFs in 3D prior to the start of reprogramming (3 days or 6 days as indicated). (**F**) Bright-field images of hDF microspheres maintained in fibroblast media. (**G**) Diameter measurements of 3D hDF microspheres ($n = 20$) maintained in fibroblast media. ****$P < 0.0001$, unpaired t test between days 1 and 8. (**H**) Live (Calcein-AM) and dead (EthD-1) staining of fibroblasts maintained for 8 days in fibroblast media in 3D or conventional 2D culture. (**I**) RT-qPCR gene expression analysis of *MKI67* and *CASP3* in hDFs cultured in 2D and 3D for 8 days. (**J**) Immunocytochemistry for Ki67 and CASP3 of day 8 hDFs cultured in 2D and 3D.

with respect to hDFs identified 4333 up-regulated and 2867 down-regulated genes (adjusted $P < 0.01$ and $\log_2$ fold change > 1) (Fig. 3G). Analysis of 14 representative fibroblast-associated genes and 21 neuronal genes confirmed successful conversion of cell identity (Fig. 3H). Notably, analysis of nine genes enriched in midbrain DA neurons revealed positive trend toward DA fate acquisition inside 3D-iDANs starting at the early time points. In addition to DA neurons, expression of genes related to glutamatergic and GABAergic neurons was also found to increase during reprogramming. Furthermore, analysis of 15 genes associated with neuronal maturation confirmed progressive maturation of the reprogrammed cells.

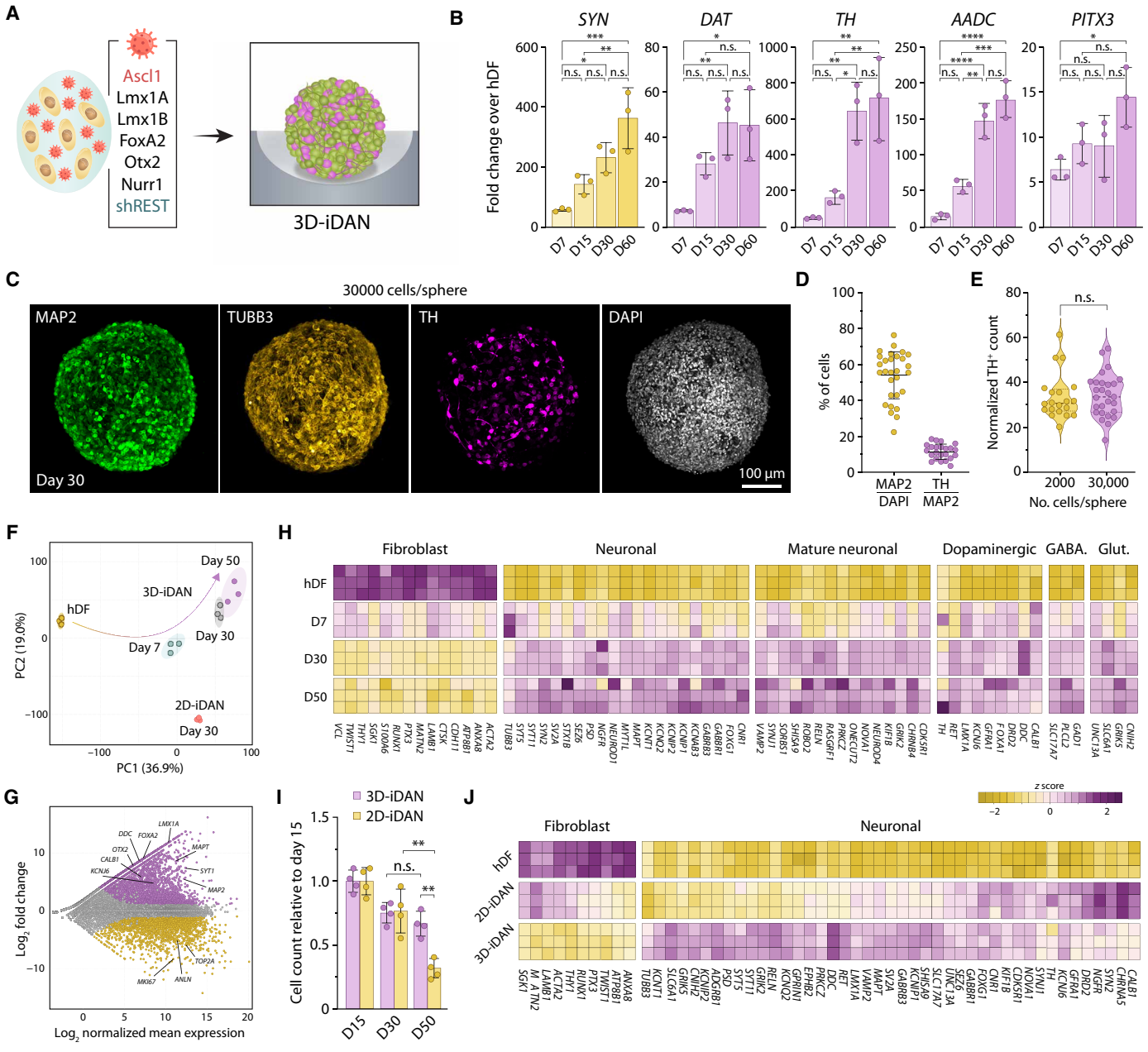

Fig. 3. Generation of 3D-iDANs. (**A**) Graphical representation of the 3D reprogramming toward DA neuronal identity. (**B**) Longitudinal RT-qPCR gene expression analysis of 3D-iDANs. Fold change with respect to hDF levels. n.s., not significant; $*P < 0.02$; $**P < 0.0096$; $***P < 0.0008$; $****P < 0.0001$, one-way analysis of variance (ANOVA). (**C**) Fluorescence immunocytochemistry of 3D-iDANs seeded with 30,000 cells per microsphere. (**D**) Quantification of the proportion of $MAP2^+$ cells from all cells and TH^+ cells from $MAP2^+$ cells. Quantification performed from three hDF lines (in total 2997 cells from 36 spheres). (**E**) Comparison of DA reprogramming efficacy between small (2000 cells per sphere seeded) and large (30,000 cells per sphere seeded) 3D-iDANs at day 30. The efficacy measurement on the *y* axis shows the number of TH^+ cells normalized to 1000 seeded cells. $n = 142$ spheres from three hDF lines. $P = 0.83$, unpaired *t* test. (**F**) PCA of transcriptomic profiles obtained from hDFs, 3D-iDANs at 7, 30, and 50 days, and 2D-iDANs at day 30 posttransduction. $n = 12$ data points. Ellipses shown with a probability of 0.95. (**G**) MA plot of differentially expressed (DE) genes (P adj < 0.01) between hDFs and day 30 3D-iDANs. Up-regulated DE genes with $\log_2$ fold change (FC) > 1 shown in purple; down-regulated DE genes with $\log_2$ FC < -1 shown in yellow. Selected DE genes labeled with gene symbol. (**H**) Heatmap representation of expression levels of selected groups of genes. Values log transformed and scaled by the mean expression of each gene across samples. (**I**) Cell survival comparison between 3D-iDAN and 2D-iDAN cultures at three different time points. The *y* axis shows the nuclear count normalized to the mean value at day 15. $**P < 0.0027$, one-way ANOVA. (**J**) Heatmap representation of expression levels of selected groups of genes for hDFs and reprogrammed cells in 3D and 2D at day 30.

Next, we applied a two-step regression strategy (maSigPro) to identify clusters of significant genes with similar expression patterns along the experimental time course (*27*). The analysis yielded nine clusters (fig. S3) that were grouped into three groups according to distinct features of temporal expression dynamics (fig. S4). The first group (1804 genes) contained clusters characterized by steadily increasing up-regulation where Gene Ontology (GO) analysis revealed terms related to neuronal processes such as synapse organization, synaptic transmission, and regulation of membrane potential. The second group (792 genes) was characterized by an "early on" pattern and steeper increase within the first week of reprogramming and GO terms relating to fate change. The third group (1108 genes) contained clusters that were down-regulated. GO analysis of the down-regulated genes revealed terms such as collagen metabolic processes, actin filament–based processes, response to wounding, and blood vessel development, thus confirming the loss of fibroblast-associated properties. Notably, GO analysis revealed that there was an up-regulation of genes related to neuron cell-cell adhesion, an important aspect of 3D culture, whereas genes related to cell-substrate interaction were down-regulated.

We then compared 3D-iDANs with established 2D reprogramming approaches and observed that there was no significant difference in cell survival at early time points, but the robustness of 3D culture became apparent in long-term cultures. Thus, at day 50, there were 66 ± 10% surviving cells in 3D cultures whereas 2D cultures contained only 31 ± 7% surviving cells (Fig. 3I and figs. S2D and S5). These results reinforce a commonly observed issue relating to 2D cultures, where cells gradually detach from their plating substrate when maintained long-term. In contrast, 3D cultures provide increased cell-cell interactions that reduce loss of cells over time. Furthermore, in comparison to a conventional 2D conversion protocol, 3D-iDANs displayed a more complete population switch to a neuronal cell identity. For example, whereas 10 fibroblast-associated genes were robustly down-regulated in 3D-iDANs, 2D-iDANs show the comparable level of down-regulation only in ~30% of these genes (Fig. 3J, left). Similarly, we observed more consistent up-regulation across a panel of 43 genes associated with neuronal identity in 3D-iDANs versus their 2D counterpart (Fig. 3J, right).

We next performed single-nucleus RNA sequencing (snRNA-seq) on 3D-iDANs (day 30) derived from three different adult hDF donors (from 55 to 75 years of age) to further investigate the cellular identities present in the spheroids. Dimensionality reduction and clustering revealed four distinct clusters: one fibroblast-like cluster, two partially reprogrammed (PR1 and PR2) clusters, and one neuronal cluster (Fig. 4A, left). Each of the four clusters was represented across the three hDF lines, with some variation in the proportion of cells in each cluster, reflecting differences in neuronal reprogramming efficiencies between the lines, ranging between 51.26 and 76.20% (Fig. 4A, right). Violin plots of key neuronal (*MAP2*, *MAPT*, *SYP*, and *NCAM1*) and fibroblast (*VIM* and *COL1A1*) markers highlighted the separation of reprogrammed and nonreprogrammed cells (Fig. 4B). To assess the identity of the neuronal cluster, we applied label transfer from ventral midbrain DA progenitors derived from human embryonic stem cells grafted into the striatum of adult rats (*28*). This analysis predicted that the neuronal cluster was composed of neurons, whereas the remaining clusters were predominantly composed of cells with fibroblast-like molecular signatures (fig. S6A). A heatmap of top markers showed heterogeneity within the neuronal cluster, indicating

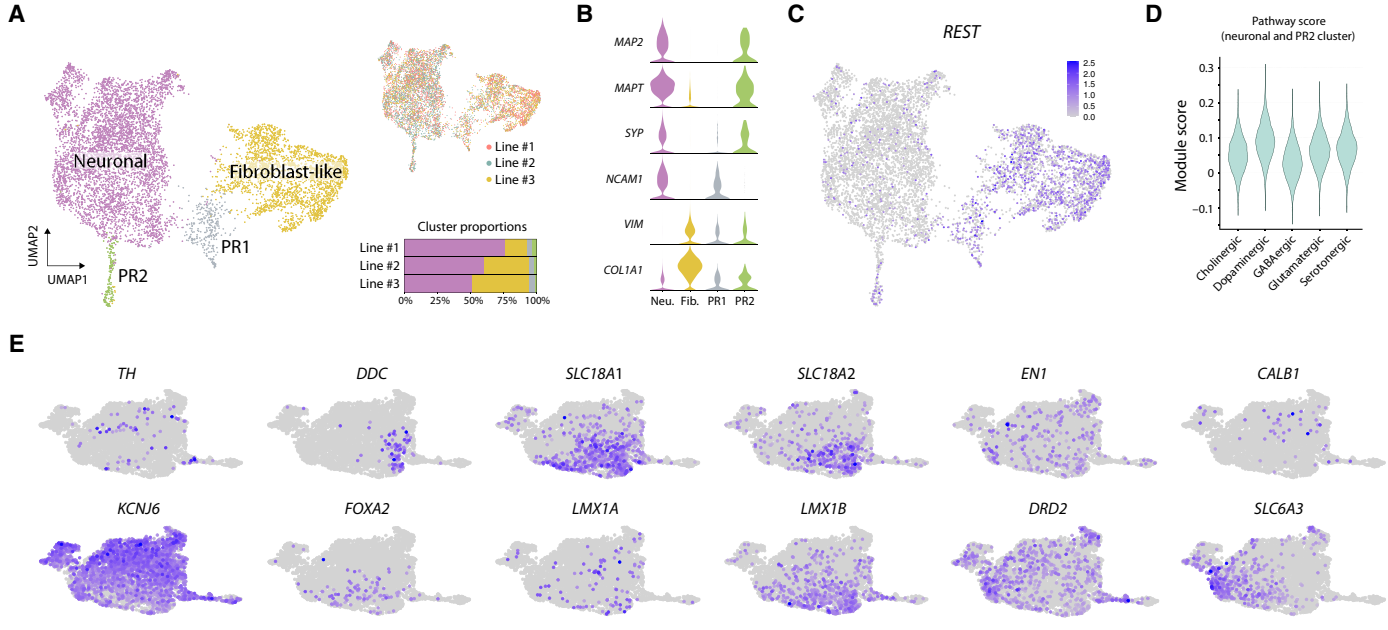

Fig. 4. snRNA-seq analysis of 3D-iDANs. (**A**) UMAP visualization of 3D-iDAN cultures at day 30 ($n = 7894$ cells) from three different adult hDF lines colored by cluster or cell line. Bar plot visualizes cluster proportions for each line. (**B**) Violin plots showing the expression level of pan-neuronal and fibroblast genes in each cluster. (**C**) Feature plot of *REST*, key gene that distinguishes fibroblast-like and partially reprogrammed clusters from neuronal clusters. (**D**) Violin plot of module scores on neuronal cluster of genes from Kyoto Encyclopedia of Genes and Genomes (KEGG) pathways glutamatergic synapse (hsa04724) GABAergic synapse (hsa04727), cholinergic synapse (hsa04725), DA synapse (hsa04728), and serotonergic synapse (hsa04726). $P < 2.2 \times 10^{-16}$, Kruskal-Wallis test. All pairwise comparisons are statistically significant with $P < 4.7 \times 10^{-7}$, Dunn's test with P values adjusted for multiple comparisons. (**E**) Feature plots of selected genes related to dopamine identity and presynaptic compartments in neuronal subclusters.

variability in the neuronal identity of reprogrammed cells (fig. S6B). GO analysis of top genes supported these findings, revealing that the neuronal cluster was enriched in neuronal-related pathways, whereas the fibroblast-like cluster was enriched in extracellular matrix, migration, and connective tissue development pathways (fig. S6C). PR1 cluster exhibited a muscle-like identity (fig. S6C), suggesting a potential competing reprogramming program previously described for Ascl1-indcued reprogramming (*29*, *30*). When analyzing the role of *REST* expression during reprogramming, we found that successful knockdown of *REST* distinctly separated the neuronal and fibroblast-like cells, supporting the role of *REST* in maintaining cellular identity and regulating reprogramming efficiency (Fig. 4C). We next reclustered the *MAP2* expressing clusters (neuronal and PR1 cluster) (fig. S6D). Module scoring of various neuronal subtypes revealed that the DA lineage scored the highest, indicating the DA identity of the reprogrammed neurons (Fig. 4D). Notably, feature plots of key DA genes demonstrated diverse expression within the neuronal cluster with prominent expression of markers related to DA identity and presynaptic compartments such as *KCNJ6* (GIRK2), *SLC18A1/2* (VMAT1/2), *DDC* (AADC), *DRD2*, and *SLC6A3* (DAT) (Fig. 4E). In summary, these results demonstrate that the overexpression of the six transcription factors is able to induce DA identity in the reprogrammed neurons. However, they also emphasize the need for more efficient methods that will allow effective and simultaneous delivery of all the needed reprogramming factors together with robust knockdown of the REST complex to increase DAergic conversion.

Functional in vitro assessment of 3D-iDANs

To validate that the generated neurons were functionally active in vitro, we performed whole-cell patch-clamp electrophysiological recordings in intact 3D-iDANs at 60 days postinduction. A proportion of recorded cells (6/16) displayed the ability to induce action potential (AP) upon depolarization (Fig. 5A) along with fast-inactivated inward and outward currents upon membrane depolarization, typical of voltage-gated sodium channels and delayed potassium currents (Fig. 5B). In these cells, membrane capacitance (Fig. 5C) and AP properties (Fig. 5D) indicated a maturing neuronal function. Together, we show that converted cells within 3D-iDANs can develop synaptic compartments necessary for function and fire APs upon membrane depolarization.

We also used calcium imaging to show that reprogrammed cells respond to potassium chloride (KCl) stimulation, a process that causes membrane depolarization and activation of voltage-gated channels in neurons (*31*). 3D-iDANs exhibited a sharp increase in calcium influx upon KCl addition, thus confirming the ability of the reprogrammed cells to respond to chemical stimulus (Fig. 5, E and F). To investigate whether 3D-iDANs are capable of releasing dopamine, we took advantage of a microscopy-based detection approach that uses dopamine sniffer cells expressing genetically encoded GRAB$_{DA1H}$ DA fluorescent sensor (Fig. 5G) (*32*, *33*). We first determined the sensitivity and the detection range of the sniffer cells in vitro by exposing them to increasing concentration of dopamine solution. Sniffer cells showed a dose-dependent increase in fluorescence for

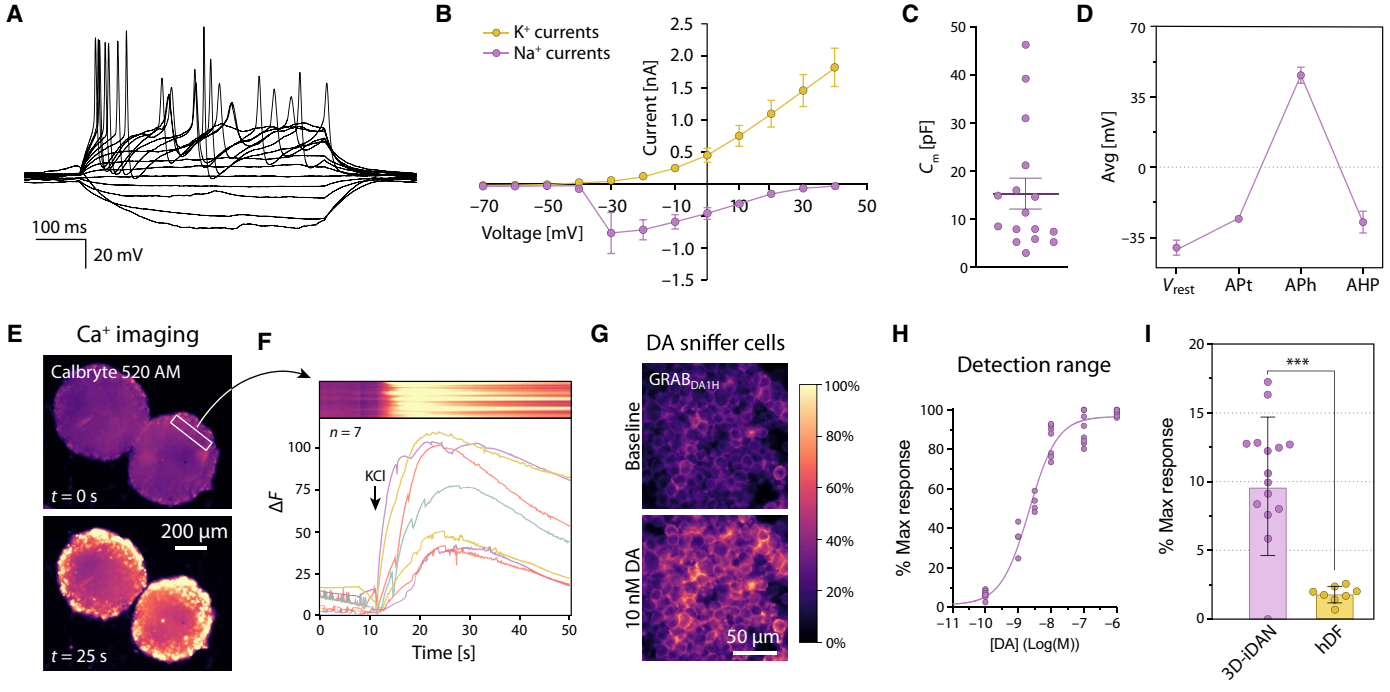

Fig. 5. Functional investigation in vitro. (**A**) Representative trace of evoked AP from a recorded 3D-iDAN cell. (**B**) Inward Na^+ and outward K^+ currents plotted against stepwise voltage induction at day 60 ($n = 7$ cells). Values are presented as means ± SEM. (**C**) Measured capacitance of recorded 3D-iDAN cells. (**D**) AP properties, resting membrane potential (V_{rest}), AP threshold (APt), AP amplitude (APh), and AHP. Each dot representing the mean value ($n = 6$). (**E**) Fluorescence images of intracellular calcium before and after stimulation of 3D-iDANs with KCl. (**F**) Kymograph (top) showing the fluorescence intensity change within the selected region of interest and traces of change in fluorescence intensity over time for whole 3D-iDAN. (**G**) Representative images of GRAB$_{DA1H}$ sniffer cells before and after stimulation with 10 nM DA solution. (**H**) Dose-response curve for the GRAB$_{DA1H}$ sniffer cell line. Fluorescence response measurements presented as the percentage of the maximum response from the baseline level. (**I**) Quantification of DA released from 3D-iDANs (from three hDF lines) after KCl stimulation as well as nonreprogrammed hDF microspheres (control). ***$P = 0.0002$, unpaired t test.

dopamine concentrations between 100 pM (6.5 ± 2% maximum response) and 10 nM (85.4 ± 8% maximum response) (Fig. 5H). We then triggered dopamine release from 3D-iDANs through KCl stimulation, and the solution from depolarized neurons was then harvested and added on top of sniffer cells. Dopamine from 3D-iDANs could be detected (9.8 ± 5% maximum response) at a level corresponding to ~200 pM (Fig. 5I).

Generation of induced assembloids

Direct neuronal reprogramming inside suspension 3D microcultures, in contrast to traditional 2D cultures, provides the opportunity for fusion and functional integration of different neuronal populations similar to what has been done with organoids (*34*). To demonstrate this, we placed a conventional 3D-iN in contact with a 3D-iDAN (Fig. 6, A and B). To determine the optimal time point for sphere fusion, we placed spheres in contact with one another at different days after the initiation of neuronal reprogramming. Day 7 spheres already showed signs of interaction after a few hours in contact (5% fused, $n = 60$). After 3 days, 83% of these pairs fused and after 5 days there was a 98% success rate (Fig. 6C). Day 14 spheres showed less plasticity with only 75% ($n = 35$) of the pairs fusing successfully after 5 days in contact. Day 21 spheres showed insufficient ability to interact with each other with no fused pairs after 5 days of contact ($n = 8$), indicating a decrease in plasticity in a much more rapid way in comparison to their stem-cell derived counterparts, which can be connected even after 120 days in culture (*35*). On the basis of these data, we therefore proceeded with fusing the spheres 7 days after the reprogramming onset. Two weeks after fusion, induced assembloids displayed a rich neuronal network with neurons crossing the interface between the two fused spheres (Fig. 6D, left). Almost all DA neurons were still located on the 3D-iDAN side of the induced assembloid, indicating that reprogrammed neurons, during this time frame, do not migrate substantially to the adjacent sphere (Fig. 6D, right). This is an important aspect because the assembloid platform should not become a homogeneous mix but rather a regionally segregated entity that would allow for investigation or manipulation of the defined regions. At the same time, the assembloids need to display synaptic connections between the regions. To demonstrate axonal connectivity, we took advantage of monosynaptic tracing technology based on retrograde transfer of glycoprotein deleted (ΔG) rabies virus across synapses (*36*, *37*). At day 0, one set of spheres (termed *source* in the assembloid) were transduced with lentivirus containing the rabies helper construct under the synapsin promoter. At day 7, these spheres were fused with spheres that did not contain the rabies helper construct (termed *target*). Then, at day 21, ΔG rabies virus was added to the culture. This results in expression of nuclear green fluorescent protein (GFP) and cytoplasmic mCherry in ΔG rabies infected *source* neurons. At the same time, retrograde transmission of rabies virus across synapses would transfer expression of cytoplasmic mCherry (but not GFP) in any *target* neurons that form presynaptic contacts directly with *source* neurons (Fig. 6E). Immunocytochemistry performed on traced day 28 assembloids confirmed synaptic connections between the fused spheroids (Fig. 6F). Although *source* neurons were positive both for nuclear GFP and mCherry, we identified $mCherry^+/GFP^-$ cells with intricate neuronal morphology throughout the target side of the induced assembloid (Fig. 6G).

Intracerebral transplantation into the adult rat brain

The major goal of this work was to enable the successful engraftment of neurons directly converted from adult hDFs into the adult brain environment (Fig. 7A), which has not been achieved up to date. To test whether the 3D reprogramming platform successfully overcomes this bottleneck, we followed the standard procedure for intracerebral transplantation into dorsolateral striatum and analyzed the outcome 4 weeks posttransplantation (Fig. 7B). To achieve this, 3D-iDANs with 2000 cells per sphere were gently harvested from their microwells and taken up into a glass capillary routinely used for intracerebral injection of stem cell–based cell suspensions (Fig. 7C) (*38*). The use of a narrow capillary (~150 μm in inner diameter) is important as it minimizes the invasiveness and the trauma of the transplant procedure itself.

In the first experiment, we compared the survival of 3D-iDANs and 2D-iDANs. Fluorescence immunostaining for human nuclei (HuNu) in transplanted brain slices revealed a significant increase in survival of human cells reprogrammed in 3D (2278 ± 1066 counted nuclei) in comparison to enzymatically harvested cells from 2D cultures where graft survival was minimal (107 ± 69 counted nuclei) (Fig. 7D). Immunostaining for the human neuronal marker neural cell adhesion molecule (hNCAM) indicated even bigger differences between the two conditions. Although 2D culture yielded a small number of unhealthy-looking cells lacking neuronal morphology, transplanted 3D-iDANs generated neuron-rich grafts that span multiple brain sections with compact cell bodies and thin projections emanating into the host tissue (Fig. 7, E to H). DA neurons (TH^+) were also found inside the graft, indicating survival of this neuronal population, which is considered particularly fragile (Fig. 7I). Fluorescence immunocytochemistry of 3D-iDAN grafts revealed surviving neurons positive for the additional DA markers GIRK2 and ALDH1A1 (fig. S7).

Then, we compared the transplantation outcome of small (2000 cells per sphere) and large (30,000 cells per sphere) 3D-iDANs. Large 3D-iDANs require the use of a bigger capillary that leads to more host damage at the time of grafting, and they also produce suboptimal grafts. Grafts from larger 3D-iDANs were riddled with pockets devoid of cells, which most likely arise from a low packing capability that leaves empty spaces between adjacent spheres. Furthermore, visibly fewer neuronal fiber outgrowths extended from these grafts into the host tissue (Fig. 7J). Measurements of outward projection density confirmed that smaller 3D-iDANs yielded grafts with 2.5 times more projections per millimeter of graft circumference than larger 3D-iDANs (Fig. 7K).

Host integration and long-term graft survival

To assess the functional properties of the transplanted adult hDF-derived neurons, we performed whole-cell patch-clamp recordings on coronal acute brain slices at 60 days posttransplantation. hDF-derived neurons were labeled with GFP for identification (Fig. 8A). In total, 15 GFP-positive cells were patched for intrinsic membrane properties and demonstrated the resting membrane potential (V_{rest}) of −31.7 ± 7.90 mV, an input resistance (R_i) of 4.1 ± 2.3 megohms, and a capacitance (C_m) of 7.38 ± 2.49 pF, which indicated different stages in functional maturity that was much improved from the in vitro condition (Fig. 8, B and C). This was further confirmed in their intrinsic firing properties with 40% of the cells that were able to generate multiple APs indicative of a neuronal maturity (Fig. 8, D and E),

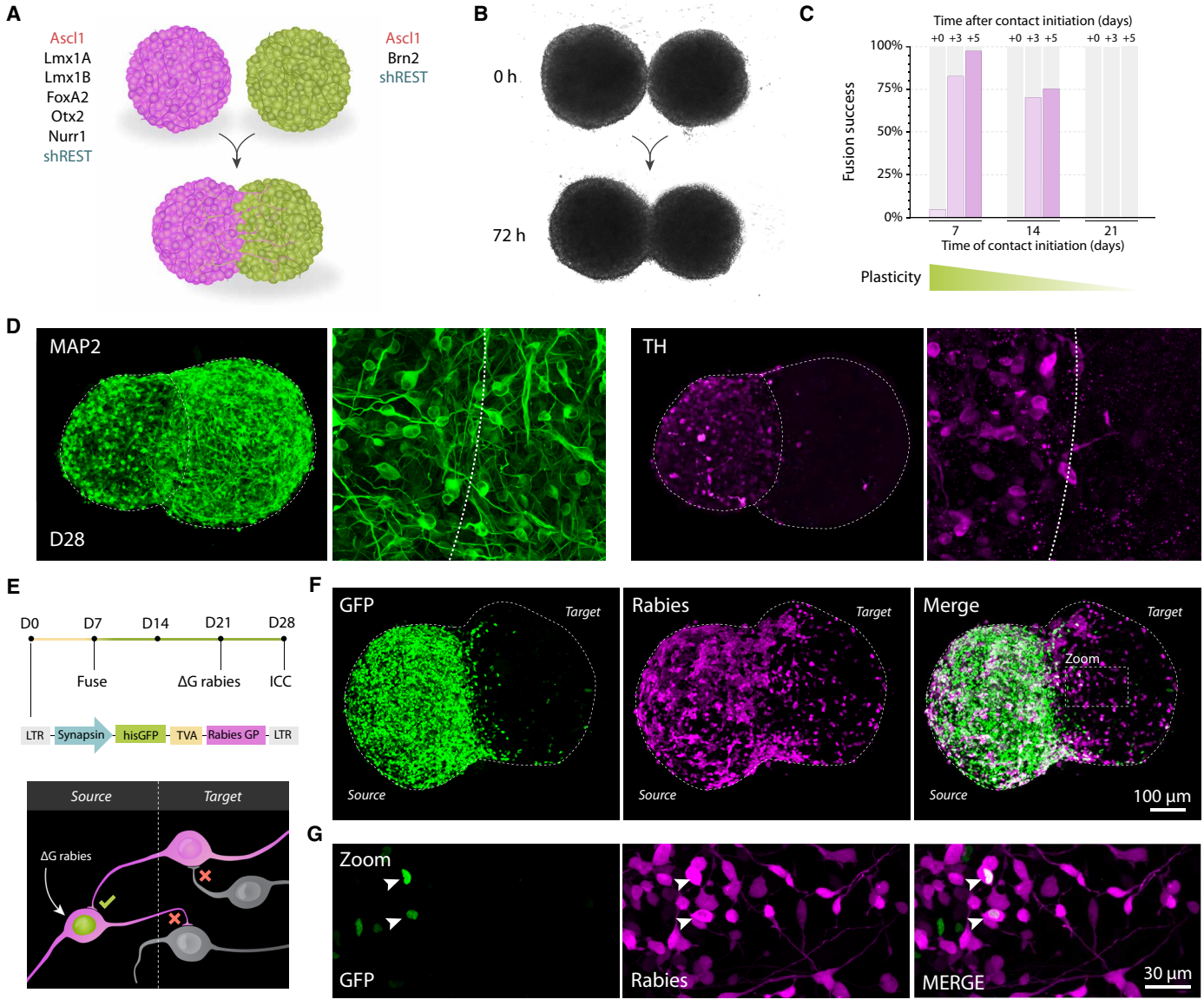

Fig. 6. Induced assembloids. (**A**) Schematic illustration of the concept behind the generation of induced assembloids. Individual microspheres first undergo direct neuronal reprogramming and are then fused together. (**B**) Bright-field images displaying fusion of two (day 7) microspheres 72 hours after they are placed in contact. (**C**) Bar graph displaying success rate of microsphere fusion with respect to the day of first contact (days 7, 14, and 21) and time after contact initiation (+0, +3, and +5). Loss of plasticity indicated by the green gradient. (**D**) Confocal fluorescence image of neuronal marker MAP2 and DA marker TH in induced assembloid at day 28 after the initiation of conversion. Spheres were fused at day 7. The image displays a maximum intensity projection from a 219-µm-thick optical slice. (**E**) Schematic illustration displaying the experimental setup and underlying principles of transsynaptic retrograde rabies tracing experiment. (**F** and **G**) Representative confocal fluorescence images displaying synaptic connections between two spheres in an induced assembloid. The source neurons ($GFP^+/mCherry^+$) are present in the left half of the assembloid that was transduced with the rabies helper construct. Nontransduced right assembloid half shows traced neurons ($GFP^-/mCherry^+$) that formed synaptic connections with the neurons in the adjacent source sphere.

another 40% only fired single AP indicative of immature state, and 20% of the cells showed no AP in response to steps of depolarization (fig. S8A). Further analysis of the AP properties revealed an AP threshold of −23.1 ± 8.56 mV, AP amplitude of 40.70 ± 5.03 mV, and after-hyperpolarization (AHP) of 12.93 ± 2.12 mV (Fig. 8B). These properties resemble those of cultured hDF-derived neurons (*9*, *18*), including low maximum sodium (80.1 ± 14.2 pA) and potassium (441.9 ± 76.6 pA) currents evoked by increasing steps of depolarization in voltage clamp mode (Fig. 8F). Tetrodotoxin (TTX) blockade further confirmed the sodium channels activation (fig. S8B). We observed spontaneous APs in 20% of recorded cells (Fig. 8G), typical of DA neurons, that has not yet been observed in vitro (*39*).

To assess integration of transplanted 3D-iDANs into the host circuitry, we took advantage of the same monosynaptic rabies tracing technology used to analyze induced assembloids. First, at the time of seeding into microwells, hDFs were transduced with lentivirus

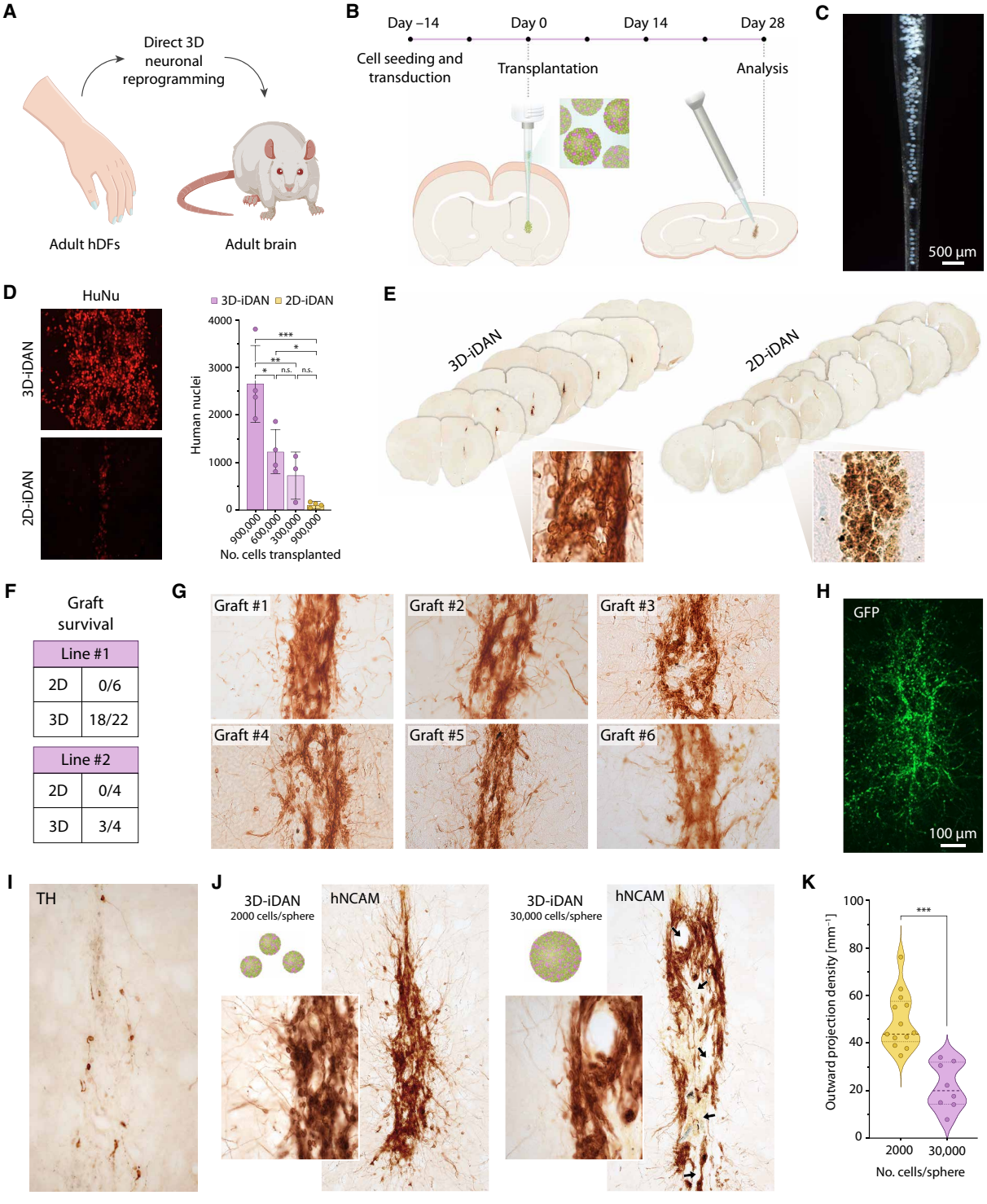

Fig. 7. Intracerebral transplantation of 3D-iDANs into the adult rat brain. (**A** and **B**) Graphical representation of the experimental timeline. (**C**) Image showing collected 3D-iDANs in a glass capillary, prepared for minimally invasive transplantation into the adult rat striatum. (**D**) Comparison of surviving human cells (marked by HuNu) between 3D-iDANs and 2D-iDANs. Representative fluorescence images accompany the graphs. Counting performed in one slice of eight from the series. $*P < 0.055$; $**P = 0.003$; $***P = 0.0002$, one-way ANOVA. (**E**) Images of a series of consecutive rat brain slices with DAB staining for human-specific neuronal marker hNCAM showing the graft size and cellular morphology for the two conditions. (**F**) Quantification of animals where the surviving graft was identified. (**G**) DAB staining for hNCAM showing six representative images of the surviving 3D-iDAN grafts. (**H**) Confocal fluorescence image of cells in the graft labeled with SYN-GFP. (**I**) DAB staining for TH showing surviving induced DA neurons. (**J**) Comparison between grafts from large (30,000 cells per sphere) and small (2000 cells per sphere) 3D-iDANs 4 weeks posttransplantation. For both cases, the same total number of cells was transplanted. (**K**) Analysis of outward projection density shows that grafting of small 3D-iDAN yields a significantly larger number of projections that grow out into the host tissue. $***P = 0.0001$, unpaired *t* test.

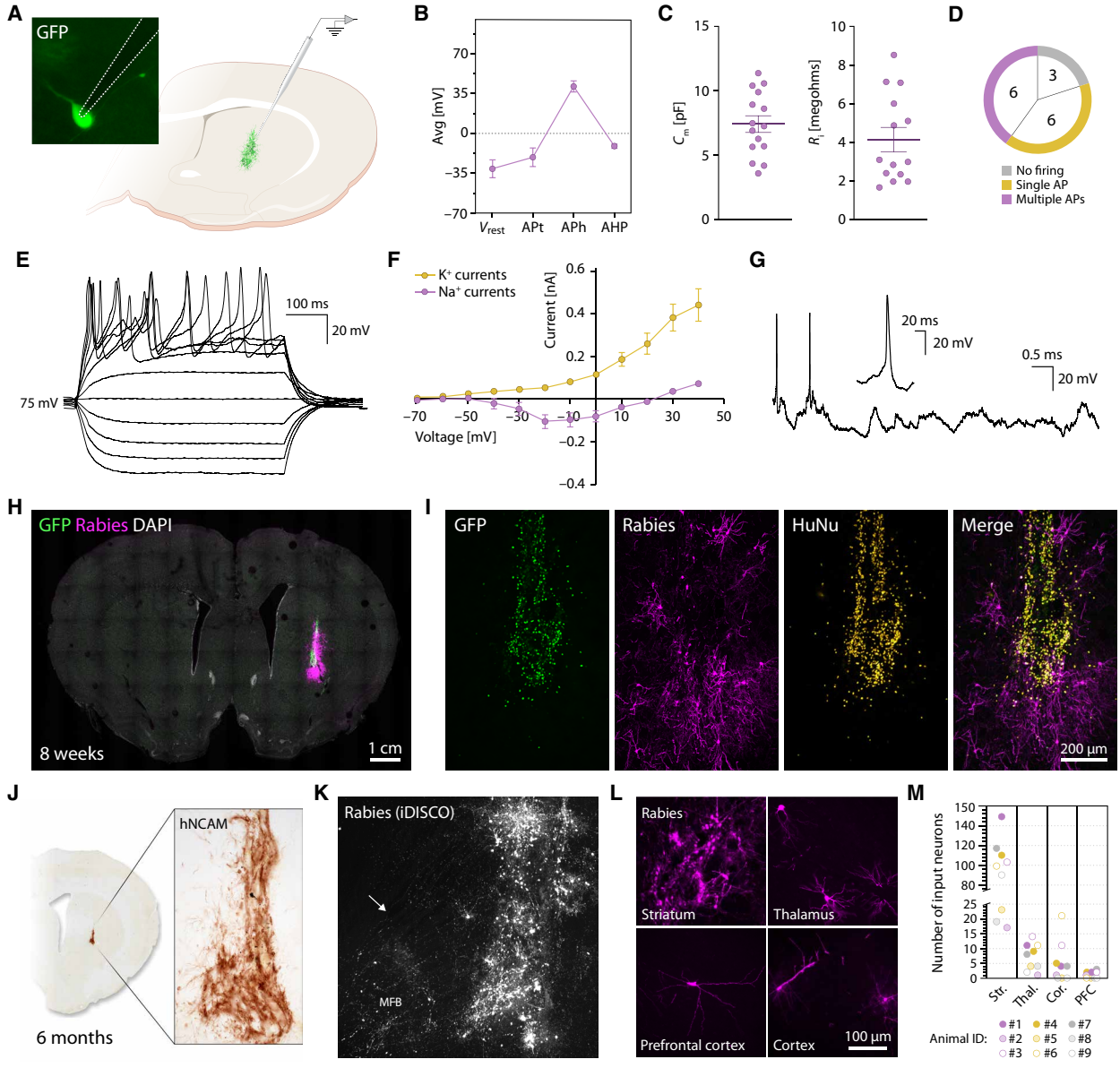

Fig. 8. Posttransplantation assessment of functional activity and host integration. (**A**) Graphical illustration and fluorescence image showing the micropipette tip accessing a GFP-labeled neuron in an acute brain slice of rat dorsolateral striatum. (**B**) Properties of the first observed AP evoked by the rheobase current injection step such as resting membrane potential (V_{rest}), AP threshold (APt), AP amplitude (APh), and AHP. (**C**) Summary of capacitance (C_m) and input resistances (R_i) of transplanted 3D-iDAN neurons. (**D**) Proportion of recorded cells firing none, single, and multiple APs (**E** and **F**) Representative voltage responses to depolarizing and hyperpolarizing currents. (**G**) Example of spontaneous APs firing recorded in a current clamp at holding potential of −70 mV. (**H**) Fluorescence confocal image of a whole brain slice showing an 3D-iDAN graft, 8 weeks postgrafting. Transplanted cells are marked with nuclear GFP. Host cells making synaptic connections with the graft are labeled with (ΔG) rabies virus (magenta). (**I**) Close-up fluorescence image of the same graft with the addition of HuNu staining confirming that the GFP-labeled cells are of human origin. (**J**) Overview image and a close-up of hNCAM-DAB staining in a striatal brain slice. (**K**) Maximum intensity projection from a series of fluorescence light sheet images showing rabies-traced host-to-graft synaptic inputs. Anatomical landmarks were identified from endogenous background signal. (**L**) Fluorescence confocal images of rabies-traced neurons in different brain regions 24 weeks posttransplantation. (**M**) Quantification of input neurons per brain region. Counting performed on one section set from a series of eight.

containing rabies helper construct. Then, a week before the animals were euthanized for analysis, they were injected with ΔG-rabies virus at the location of the graft. This resulted in expression of nuclear GFP and cytoplasmic mCherry in grafted *source* cells. Retrograde transmission of rabies virus across synapses would induce expression of mCherry (but not GFP) in any host neurons that form a presynaptic contact directly with grafted human iNs—*target*. Fluorescence staining of brain slices 8 weeks posttransplantation confirmed host-to-graft connectivity (Fig. 8H). Nuclei positive for GFP were also positive for HuNu, confirming that these are human neurons originating from grafted 3D-iDANs. A network of mCherry$^+$/GFP$^-$ neurons with complex morphology surrounded the graft,

indicating that neurons directly reprogrammed from adult hDFs were not only able to survive the transplantation but also received synaptic inputs from the host (Fig. 8I).

Last, we assessed the potential of human neurons from transplanted 3D-iDANs to survive over long periods of time (at least 24 weeks) while maintaining communication with host circuitry. hNCAM-DAB (3,3′-Diaminobenzidine) immunohistochemistry of striatal brain slices from rats euthanized 24 weeks posttransplantation show neuron-rich grafts with dense neuronal projections, a sign of morphological maturation of the transplanted cells (Fig. 8J). We then performed iDISCO tissue clearing and light sheet microscopy of whole rat brains with grafts labeled for monosynaptic rabies tracing (Fig. 8K). The results show that cells providing input to the transplanted cells are not only residing in the local host environment. Closer analysis of immunostained brain slices revealed endogenous neurons from several brain regions including the thalamus, prefrontal cortex, and cortex, making connections with the grafted cells in addition to striatal host circuitry (Fig. 8L). Quantification of input neurons per brain region revealed that most connections were formed locally in striatum, whereas fewer input neurons were detected in the other three brain regions (Fig. 8M).

DISCUSSION

Increasingly sophisticated stem cell–based 3D culturing techniques for neuroscience applications have shown great potential to overcome many of the inherent limitations of the traditional 2D approaches and to mimic aspects of the native tissue such as spatial organization, cell-cell interactions, mechanical properties, and extracellular environment (*40*, *41*). However, novel culturing platforms in 3D for direct neuronal reprogramming remain largely unexplored (*22*). Instead, major efforts in the field have been directed toward understanding the underlying molecular mechanisms of direct fate change as well as developing ever more complex combinations of transcription factors, microRNAs (miRNAs), and small molecules for more efficient generation of type- and subtype-specific neural cells (*42*). Here, we demonstrated that the 3D conditions have a significant effect on the neuronal reprogramming process as well as on the viability and function of the iNs. Most notably, we show that reprogramming in 3D results in transplantable neurons that survive, integrate, and functionally mature after transplantation into the adult rat brain.

Neural conversion in 3D offers several advantages over 2D conversion protocols. It does not rely on artificial cell-substrate interactions, which are well known to be unstable over long culture periods (leading to cell detachment and loss), but rather on reinforced cell-cell interactions that facilitate long-term neuronal survival and maintenance in vitro. Although a 3D environment benefits neuronal culture, fibroblasts are anchorage-dependent cells whose function and maturation are dependent on cell–extracellular matrix interactions (e.g., collagen type I). When devoid of these cues, fibroblasts undergo gene expression changes and require an extensive selection process to become suspension adapted (*43*). Our results demonstrate that, in suspension microcultures, viability of hDFs decreases significantly within days. Suspension 3D microcultures, therefore, might provide negative selection pressure on the nonconverted cells. Mechanical cues in 3D microcultures could also play a role in promoting neuronal reprogramming and function. In comparison to hard tissue culture plastic, self-assembled 3D microculture (albeit dominated by cell-cell interactions) provides a soft environment that has been shown to promote direct neuronal reprogramming (*22*, *44*).

The potential benefits of direct neural conversion within the field of neuroscience are significant and varied, with particular advantages in areas of modeling late onset neurodegenerative diseases due to the maintenance of donor age in the reprogramming process (*12*, *14*, *45*, *46*). It is also an interesting candidate for cell-based therapies, in particular autologous therapies, as direct conversion bypasses the pluripotent stage, which helps mitigate the risk of teratomas or other unwanted cell proliferation after transplantation. For these applications, however, it is necessary to generate subtype-specific neurons of relevance for a particular disease. Although it is possible today to generate a number of neuronal cell types, in this study, we tested the possibility to generate DA neurons via 3D conversion by adding conversion factors previously shown to result in DA neurons when adult dermal fibroblasts are converted in 2D (*14*). We show that also during 3D conversion, these factors resulted in the generation of neurons with a gene and protein expression profile of DA neurons, with functional properties including the documented ability to produce and release DA. At the same time, our results indicate that the expression of conversion factors in the right combination remains the main driving force behind cell identity change. Therefore, generating subtype-specific neurons such as DA neurons with higher efficacy and fidelity would require designing less complex and more efficient reprogramming systems. The current state-of-the-art DA reprogramming conditions used in this study uses eight separate lentiviral particles (six for transcription factor overexpression and two for *REST* suppression). The use of multiple vectors reduces the likelihood of a high number of cells expressing all the reprogramming factors, which affects the yield of subtype-specific neurons.

An inherent benefit of a self-supported suspension microculture is the ability of manipulation without the need for enzymatic or mechanical dissociation of cells. This aspect has two major experimental advantages as shown in this study. First, it provided a way of combining separately reprogrammed microspheres into induced assembloids within a defined time window of maintained cellular plasticity. This paves the way for studies of interregional brain communication, neuron-glia interaction, pathology transfer, and disease modeling in vitro, in a similar manner to that which has been done using stem cell–generated brain assembloids (*34*, *47*). Second, we used the developed approach to transplant 3D-iDANs reprogrammed from adult hDFs into the adult rat brain. This study shows the successful demonstration of transplanting reprogrammed neurons from adult donors into the adult brain. The transplanted cells survived, functionally matured, and integrated into host circuitry with presynaptic partners identified in the striatum, thalamus, prefrontal cortex, and cortex of the host brain. The ability to generate transplantable iDANs presents an important achievement toward in vivo studies using patient-specific iNs as well as for exploring reprogrammed neurons in cell replacement therapies based on direct cell reprogramming.

Our findings are supported by recent studies that demonstrated the benefit of the 3D environment for direct glia-to-neuron conversion (*48*) as well as miRNA-mediated direct hDF reprogramming into cortical neurons inside 3D hydrogels for modeling of late-onset neurodegeneration (*45*) where the 3D environment is key to investigating the extracellular pathological deposits. The data also reinforced findings that cellular organization into self-supported 3D structures mitigates mechanical and biological stresses and, by doing so, increases cell survival and preserves cell function (*21*, *49*, *50*).

Although we focused on the generation of DA neurons inside 3D microcultures, the presented approach is highly versatile and could easily be adapted to conversion strategies already established in 2D for direct reprogramming of fibroblasts to other neuronal [e.g., cholinergic (*6*), striatal medium spiny neurons (*51*), and motor neurons (*52*)] and nonneuronal cell types (e.g., astrocytes (*53*–*55*) and oligodendrocytes (*56*, *57*)]. Thus, the presented approach for 3D direct conversion of transplantable neurons from hDFs has widespread potential for disease modeling and regenerative medicine applications and, due to its simplicity and versatility, could readily be adapted to different neuronal subtypes and diseases.

MATERIALS AND METHODS

Cell lines

hDF lines #1 (C11) and #3 (C7) were obtained from the Parkinson's Disease Research Clinic at the John van Geest Centre for Brain Repair (Cambridge, UK) and used under full local ethical approvals: REC 09/H0311/88 (University of Cambridge). hDF line #2 (AST) was obtained from the University College London Queen Square Institute of Neurology biobank. The subjects' consent was obtained according to the declaration of Helsinki. For biopsy sampling information, see (*20*).

Cell culture

hDFs were cultured on uncoated T175 flasks in fibroblast medium [Dulbecco's modified Eagle's medium (DMEM), 10% fetal bovine serum (FBS), and 1% penicillin-streptomycin] at 37°C and 5% CO_2. All media were changed every 2 to 3 days. Upon reaching a 90% confluency, the cells were split with 0.05% trypsin in Dulbecco's phosphate-buffered saline (DPBS) and further expanded, frozen down, or replated for reprogramming experiments. Fibroblasts replated for reprogramming in 2D were seeded onto poly-ornithine, laminin, and fibronectin-coated plates at a density of 25,000 cells/cm^2 according to our previous study (*24*). The following day, the media were replaced with fresh fibroblast media containing the virus. For iN reprogramming, a polycistronic vector containing *Ascl1*, *Brn2*, and sh*REST* was used at an multiplicity of infection (MOI) of 20. For iDAN reprogramming, eight vectors were used (single vectors for each transgene: *Ascl1*, *Nurr1*, *Lmx1A*, *Lmx1B*, *FoxA2*, and *Otx2* and two vectors for sh*REST*) at an MOI of 5 per construct. To ensure a more homogeneous transduction of cells in 3D cultures, the cells were seeded together with the virus in ultralow attachment plates: For 250 to 5000 cells per sphere, Elplasia plates (Corning) were used; for more than 5000 cells per sphere, Costar U-bottom ULA 96-well plates (Corning) were used. Two days later, the media were changed to early neuronal conversion medium consisting of NDiff227 supplemented with CHIR99021 (2 μM), SB431542 (10 μM), Noggin (0.5 μg/ml), LDN1931189 (0.5 μM), VPA (1 mM), LM22A4 (2 μM), GDNF (2 ng/ml), NT3 (10 ng/ml), and db-cAMP (0.5 mM). Partial media changes were carried out two to three times per week until day 16 when the media were changed to late neuronal conversion media made up of NDiff227 supplemented with LM22A4 (2 μM), GDNF (2 ng/ml), NT3 (10 ng/ml) and db-cAMP (0.5 mM). Media were partially changed every 2 to 3 days until the end of the experiment. The abovementioned media composition and media change schedule apply both to 3D-iN and 3D-iDAN conversions.

Lentivirus production

The lentiviral particles were produced in human embryonic kidney (HEK) 293T cells according to a previously published protocol (*58*). In brief, HEK293T cells were transfected with three helper packaging plasmids along with the plasmid of interest and polyethylenimine (PEI) to facilitate transfection. After 48 hours, the media were filtered, ultracentrifuged, and resuspended in DPBS. The titer was determined by RT-qPCR using primers against a reference gene (*ALB*) and a virus-specific gene (*WPRE*) and comparing the expression to a reference virus with an already measured titer.

In vitro whole-cell patch-clamp

Electrophysiological recordings were performed 50 to 60 days postinduction on intact spheres transferred into the recording chamber at experimental time point. The chamber was filled with Krebs solution gassed with 95% O_2 and 5% CO_2 at room temperature (RT). The composition of the Krebs solution was as follows: 119 mM NaCl, 2.5 mM KCl, 1.3 mM $MgSO_4$, 2.5 mM $CaCl_2$, 25 mM glucose, and 26 mM $NaHCO_3$ with the pH adjusted to 7.4. Spheres were recorded in a free-floating state using a Multiclamp 700B amplifier (Molecular Devices, San Jose, CA, USA) with borosilicate glass pipettes (3 to 7 megohms) backfilled with the following intracellular solution: 122.5 mM potassium gluconate, 12.5 mM KCl, 0.2 mM EGTA, 10 mM Hepes, 2 mM MgATP, 0.3 mM Na_3GTP, and 8 mM NaCl adjusted to pH 7.3 with KOH. pClamp 10.2 (Molecular Devices, San Jose, CA, USA) was used for data acquisition with the current filtered at 0.1 kHz and digitized at 2 kHz. Directly after successful break in, the resting membrane potential was measured in current-clamp mode, followed by current injection to stabilize cells at −60 to −70 mV. To elicit evoked APs, current was injected from −20 to +35 pA with 5-pA increments. Measurements of inward sodium and delayed rectifying potassium currents were done with cells clamped at −70 mV in voltage clamp mode using voltage-depolarizing steps supplied for 100 ms at 10-mV increments. Data were processed and analyzed with the Clampfit 10.3 (Molecular Devices, San Jose, CA, USA) and Igor Pro 8.04 (Wavemetrics, Portland, OA, USA) software combined with the NeuroMatic package (*59*).

Calcium imaging

3D-iDANs were incubated for 30 min at 37°C with 3 μM Calbryte 520 AM calcium indicator (AAT Bioquest) in maturation medium containing 0.02% Pluronic F-127 (Sigma-Aldrich). Cells were then rinsed with baseline buffer containing 1.2 mM $MgCl_2$, 2 mM $CaCl_2$, 150 mM NaCl, 5 mM KCl, 5 mM glucose, and 10 mM Hepes buffer, and imaging was performed on an inverted fluorescence microscope equipped with a 20x objective. Stimulated calcium influx was recorded with an exposure time of 100 ms by inducing cell membrane depolarization through the addition of stimulation buffer containing of 1.2 mM $MgCl_2$, 2 mM $CaCl_2$, 5 mM NaCl, 150 mM KCl, 5 mM glucose, and 10 mM Hepes buffer. Images were analyzed in ImageJ (NIH) and plotted in Prism (GraphPad).

DA sniffer cells

The HEK293 Flp-In T-Rex cell line (*33*), stably expressing fluorescent G protein–coupled receptor-based DA sensor $GRAB_{DA1H}$ (*32*), was cultured in DMEM supplemented with 10% FBS, blasticidin (15 μg/ml), and hygromycin B (200 μg/ml). Sniffer cells were passaged at least twice before they were used in experiments.

Forty0-eight hours before the measurements were taken, sniffer cells were seeded in imaging chambers (8-well, ibidi) coated with poly-L-ornithine and the expression of $GRAB_{DA1H}$ sensor was induced with tetracycline (1 μg/ml). Live DA sniffer cell imaging was performed on a wide-field Leica microscope using a 20x numerical aperture 1.4 objective. First, three images were obtained to determine baseline fluorescence. Then, samples collected from depolarized 3D-iDANs (or nonreprogrammed spheres as a control) were added to the imaging well and three more images were taken to determine the fluorescence response of the sensor. Images were averaged and analyzed in ImageJ (NIH) and results plotted in Prism (GraphPad).

Immunocytochemistry

3D cultures cells were washed twice with DPBS and fixed with 4% paraformaldehyde (PFA) for 30 min in RT and washed twice in DPBS before being stained according to a previously published study (*48*). In short, fixed samples were incubated in blocking solution (5% serum and 0.1% Triton) for 1 hour and then in blocking solution with primary antibodies in 4°C overnight. The following day, the cells were washed twice with DPBS, incubated in blocking solution for 30 min in RT, followed by overnight incubation with secondary antibodies in blocking solution along with 4′,6-diamidino-2-phenylindole (DAPI) (1:500). Last, the cells were washed twice and left in 4°C until analysis.

For 2D, cells were washed twice with DPBS and fixed with 4% PFA for 10 min in RT and washed twice before adding blocking solution (5% serum and 0.1% Triton in PBS) for 1 hour to prevent nonspecific binding. Next, cells were incubated with primary antibodies at 4°C overnight. The following day the cells were washed twice with DPBS, incubated in blocking solution for 30 min in RT, followed by secondary antibody solution (1:200, Jackson ImmunoResearch Laboratories) for 1 hour. Last, the cells were washed twice and left at 4°C until analysis.

Clearing of 3D cultures

Once the 3D cultures had been stained, they were cleared to improve the imaging quality and enable imaging of the entire sphere. The spheres were put in 20, 40, 60, 80, and 100% methanol for 10 min each. Next, they were left in a dichloromethane (DCM)–methanol mixture (2:1) for 1 hour and then in 100% DCM for two, 10-min periods. Last, the spheres were cleared with ethyl cinnamate and transferred to 96-well black μ-plates (ibidi, #89626).

Live-dead staining

3D and 2D fibroblast cultures were incubated with Calcein AM and Ethidium Homodimer-1 (1:500) in Hanks' balanced salt solution (HBSS) for 20 min at RT. Cultures were then washed once with HBSS before imaging on a fluorescence microscope equipped with a 20x objective.

Reverse transcription quantitative polymerase chain reaction

The cells were washed twice with DPBS and lysed, and total RNA was collected using the RNeasy Micro Kit (Qiagen, #74004) according to the manufacturer's instructions. RNA (1 μg) was reverse transcribed to cDNA with the Maxima First Strand cDNA Synthesis Kit (Thermo Fisher Scientific, #K1642). The cDNA was mixed with the primers of interest and with SYBR Green Master mix (Roche, #04887352001) using the Bravo instrument (Agilent) and analyzed by a LightCycler 480 II instrument (Roche) using a two-step protocol with a 95°C, 30-s denaturation step followed by a 60°C, 60-s annealing/elongation step for a total of 40 cycles. Samples were analyzed with the ΔΔCt method, normalized against the two housekeeping genes *ACTB* (actin-beta) and *GAPDH* (glyceraldehyde-3-phosphate dehydrogenase) and the data presented as a fold change of expression compared to nonconverted hDFs. Table S1 contains the list of primers used in the study.

Bulk RNA-seq

RNA was extracted using the RNeasy mini kit (Qiagen) following the manufacturer's instructions. cDNA libraries were prepared using the Illumina TruSeq library preparation kit and sequenced with 2×150–base pair (bp) paired-end reads on an Illumina NextSeq 2000 using the P3 flow cell (~37M reads per sample). Raw base calls were demultiplexed and converted into sample-specific fastq files using default parameters of the bcl2fastq program (v 2.20, Illumina). Trimmed reads (TrimGalore, 0.6.1) were aligned to the human genome version GRCh38 (Ensembl release 99) using STAR (*60*) (v2.7.3) and quantified using Salmon (*61*) (v0.14.0).

A PCA was performed through singular value decomposition of a data matrix that had been both centered and scaled using prcomp function in R. Identification of differentially expressed genes from gene-level count tables was performed using DEseq2 (*62*) (2.11.40.7+galaxy1). Heatmaps were generated to visualize gene expression levels by log transforming and mean scaling transcript per million (TPM) values using the heatmap.2 function in R. Assessment of significant gene expression profile differences was achieved using maSigPro (*27*) (1.49.3.1+galaxy1) on gene-level count tables. Functional analysis of differentially expressed genes, selected based on a false discovery rate–adjusted *P* value (*P* adj; using a Benjamini-Hochberg procedure) cutoff of 0.05, was conducted using Goseq (*63*) (1.44.0+galaxy0). The outcomes of this analysis were visually summarized using the REVIGO (*64*) tool. RNA age for each sample was estimated using the predict_age function in the R package RNAAgeCalc (*65*).

DNA methylation profiling

DNA was extracted from ~1000 3D-iDANs (containing 2000 seeded fibroblasts each) or from a T25 flasks (1.2×10^6 fibroblasts plated) using the DNeasy Blood and Tissue Kit (Qiagen) following the manufacturer's instructions. Bisulfite conversion of DNA samples was prepared using the EZ DNA Methylation kit from Zymo Research. Methylation analysis of bisulfite pretreated DNA samples was done using the Illumina Infinium MethylationEPIC v2.0 BeadChip (EPIC). Illumina Genome Studio software was used to perform sample quality control. We calculated individual epigenetic ages for each sample using Horvath's clock using the R package cgageR (version 0.1.0, https://rdrr.io/github/metamaden/cgageR/) after preprocessing using minfi (*66*). This method relies on the methylation data from 353 CpGs to produce a continuous value that mirrors an individual's epigenetic age.

Nuclei isolation

Nuclei isolation was performed on ice using a glass douncer containing nuclei lysis buffer [0.32 M sucrose, 5 mM $CaCl_2$, 3 mM MgAc, 0.1 mM Na_2EDTA, 10 mM tris-HCl (pH 8.0), 1 mM dithiothreitol, and 0.1% Triton X]. Homogenization was achieved by manually grinding the 3D-iDANs followed by centrifugation at 900*g* for

15 min at 4°C. The resulting nuclei pellet was resuspended in cold wash buffer [PBS containing 0.1% bovine serum albumin (BSA) fraction V and RNase inhibitors (0.4 U/μl) from Ambion and SUPERaseIn] and subsequently isolated via fluorescence-activated cell sorting (FACS) using a FACSAria III cell sorter (BD Biosciences, 100-μm nozzle). Sorted nuclei were gated based on DRAQ7 staining and event size, and ~12,000 nuclei per sample were collected in DNA LoBind tubes (Eppendorf) precoated with BSA for snRNA-seq library preparation.

Single-nucleus RNA sequencing (library generation)

Library preparation was conducted using the Chromium platform (10X Genomics, PN-120233) following the manufacturer's guidelines. Barcoded beads encapsulated single nuclei in droplets where lysis and reverse transcription occurred using poly-T primers with nucleus-specific barcodes, unique molecular identifiers (UMIs), and sequencing adaptors. After amplification, libraries were fragmented and processed according to the manufacturer's instructions. Libraries were sequenced on an Illumina NovaSeq 6000 using 2×100-bp reads for transcriptomic libraries.

Single-nucleus RNA sequencing (data processing and analysis)

Raw sequencing data were processed using the Cell Ranger software (10X Genomics). Reads were aligned to the human genome (GRCh38) via the STAR aligner integrated into the Cell Ranger pipeline. Further data preprocessing and analysis were carried out in R (v4.3.3) using the Seurat package (v5.1.0) on macOS Sonoma 14.6.1. Demultiplexing of snRNA-seq data was performed using Vireo to assign cells to donor identities based on genotype information. Genotype likelihoods were provided as input from cellSNP, enabling Vireo to resolve donor-specific cell populations and distinguish doublets or unassigned cells. Nuclei were filtered to exclude those with <500 detected genes, >1% mitochondrial content, or detected as doublets by Vireo. After log normalization, highly variable genes ($n = 3000$) were identified using Seurat's vst function, followed by PCA (50 components). Batch effects across adult hDF lines were corrected using the Harmony package (v1.2.3), and corrected embeddings were used for UMAP visualization and clustering. Clusters were defined using the Louvain algorithm (resolution = 0.1) and annotated based on canonical markers and differentially expressed genes identified with Seurat's FindAllMarkers. GO enrichment analysis was conducted to identify overrepresented biological processes. The analysis was performed using the enrichGO function from the clusterProfiler R package (v4.10.1). Genes were mapped to their corresponding Entrez IDs and analyzed using the org.Hs.eg.db (v3.18.0) annotation database for human genes. Enrichment was calculated for all GO categories, with a focus on Biological Process (BP), under a *P* value cutoff of 0.05. Label transfer from a transplantation dataset (*28*) was achieved using Seurat's FindTransferAnchors and TransferData functions.

Neuronal and partially reprogrammed 1 (PR1) clusters underwent further integration and reclustering (resolution = 0.2). To assess neuronal subtype scores, five KEGG pathways (hsa04724, hsa04725, hsa04726, hsa04727, and hsa04728) were analyzed. Genes associated with each pathway were retrieved using the keggGet function from the KEGGREST package (v1.42.0). Module scores for each pathway were computed using the AddModuleScore function in Seurat. To compare module scores across pathways, the Kruskal-Wallis test was performed, followed by pairwise comparisons using Dunn's test. The ggplot2 package (v3.5.1) was used for data visualization throughout the analysis.

Animals

All experimental procedures followed the guidelines and recommendations of the Swedish animal protection legislation and were approved by the Animal Ethics board (ethical permit no. M-8579/2017). Experiments lasting 8 weeks or less were carried out in adult female Sprague-Dawley (SD) rats from Charles River Laboratories. To keep the SDs immunosuppressed and avoid graft rejection, they were given daily intraperitoneal injections of ciclosporin A (10 mg/kg) 2 days prior to cell grafting until the end of the experiment. For experiments lasting more than 8 weeks, adult female athymic rats from Envigo were used instead. All rats weighed at least 225 g before the start of any experiment, and their weights were recorded every week to keep track of potential weight loss. All rats were housed in ventilated cages under 12-hour/12-hour light/dark cycles with free access to food and water.

Surgeries

All surgeries were carried out under general anesthesia via intraperitoneal injection of Ketaminol (45 mg/kg) and Domitor (0.3 mg/kg). Marcain (0.1 ml) was given as a local anesthesia subcutaneously. The rats were placed in a stereotaxic frame and put in a "flat head" position (vertical difference between lambda and bregma < ±0.2 mm). Unilateral lesions of 6-hydroxydopamine (6-OHDA; 3.5 μg/μl, 3 μl, and 0.3 μl/min) were placed into the medial forebrain bundle to ensure a widespread DA neuron depletion in one hemisphere. The coordinates in SDs were anterior-posterior (A/P): −4.4, medial-lateral (M/L): −1.1, dorsal-ventral (D/V): −7.8 and, for nudes, A/P: −3.9, M/L: −1.2, D/V: −7.3. Cells were transplanted 4 weeks after 6-OHDA lesions into the dopamine denervated striatum via two 2-μl deposits in a single tract. For SDs the following coordinates were used: A/P: +0.8, M/L: −2.8, D/V: −4.5/−5.5. For transplantation in athymic rats, the following coordinates were used instead: A/P: +1.2, M/L: −2.8, D/V: −4.5/−5.5. For each deposit, an injection rate of 1 μl/min with a 2-min diffusion time was used. Rabies virus was injected (3 μl, 0.3 μl/min) 1 week before the end of the experiment and was placed in the middle of the cell grafting tracts as two deposits of the same D/V coordinates (−4.0/−5.0). Postsurgery, antisedan (0.28 mg/kg) and temgesic (0.04 mg/kg) were given subcutaneously to reverse the anesthesia and serve as an analgesic, respectively.

Preparation of cells for transplantation

On the day of transplantation, cells were harvested and suspended in HBSS with 10% DNAse and put on ice until used. 2D reprogrammed cells were dissociated using Accutase (75 μl/cm^2, 10-min incubation). 3D-iDANs were harvested by gentle pipetting through a cut 1-ml tip. A total of 900,000 hDFs were reprogrammed for transplantation in each animal.

ΔG-rabies virus production

EnvA-pseudotyped ΔG-rabies virus was produced according to a previously published procedure (*37*). The titer was estimated to 10×10^6 to 30×10^6 transducing units/ml and was used at a working dilution of 5% for the experiments.

Immunohistochemistry

At the end of the experiment, the rats were administered a lethal dose of anesthesia by intraperitoneal injection of sodium pentobarbital

and perfused trans-cardinally with RT 0.9% saline for 3 to 5 min followed by ice-cold 4% PFA (pH 7.4 ± 0.2) for 5 min. The brains were manually removed from the skull and were left in 4% PFA at 4°C overnight. The PFA was removed the next day and replaced with 25% sucrose solution. After 2 to 3 days, once the brains had sunk in the sucrose solution, they were placed onto a freezing microtome and sectioned at 35-μm thickness in 1:8 series and stored in antifreeze at 4°C until the start of staining.

All brain sections were stained as free-floating sections in glass vials on a shaker. The sections were washed 3x in 0.1 M potassium-based phosphate-buffered saline (KPBS), incubated in Tris-EDTA (pH 9.0) for 30 min at 80°C to improve antigen binding and washed again 3x. Sections that were DAB stained were incubated in a quenching solution (10% H_2O_2 and 10% methanol in KPBS) for 15 min to quench endogenous peroxidase activity and washed 3x. Next, the sections were incubated for 1 hour in blocking solution (5% serum and 0.25% Triton) at RT and were afterward left to incubate in primary antibodies in blocking solution on a shaker at RT overnight. The following day, the sections were washed 2x and put in blocking solution at RT for 30 min followed by 1 hour in secondary antibodies. For immunofluorescence staining, the secondary antibodies were fluorophore-conjugated antibodies (1:200, Jackson ImmunoResearch Laboratories) whereas, for DAB staining, biotinylated secondary antibodies were used instead. The immunofluorescent sections were washed 3x, mounted onto chrome alum-gelatin–coated slides and coverslipped with PVA-DABCO with added DAPI (1:1000). The DAB sections were washed 3x and incubated in an avidin-biotin complex (ABC complex) for 1 hour and washed 3x. The sections were thereafter left to incubate in 0.05% DAB solution for 2 min before adding 20 μl of 3% H_2O_2 to allow color development. Last, the sections were washed 3x, mounted onto chrome alum-gelatin–coated slides, dehydrated in an ascending order of alcohol, cleared in xylene, and coverslipped with DPX mountant.

Whole brain iDISCO and light sheet microscopy

Two brains were processed for light sheet microscopy using the iDISCO clearing method (*67*) at 8 weeks after cell grafting. The brains were perfused with 2% ice-cold PFA for 5 min, followed by 1-hour postfixation on ice, and left stored in PBS. Divided by a midline sagittal cut, each half-brain was processed individually. They were washed in PBS 3x for 30 min and then in 20, 40, 60, and 80% methanol (in PBS) and 100% methanol, for 1 hour each. Next, the brains were incubated in a DCM-methanol mixture (2:1) overnight at RT on a shaker, followed by 2x 30 min washes in 100% methanol and lastly 1 hour at 4°C. They were bleached in 5% H_2O_2 and left on a shaker at 4°C overnight. Afterward, they were rehydrated from methanol to 20, 40, 60, 80, and 100% PBS, with 30 min for each step and washed in PBS/2% Triton X (PTx.2) 2x for 1 hour at RT, followed by a wash in PBS/0.2% Tween 20 with heparin (10 μg/ml; PTwH) 2x 30 min. Subsequently, the brains were incubated in permeabilization buffer [PTx.2/glycine/dimethyl sulfoxide (DMSO)] at 37°C for 3 to 5 days on a shaker before being washed 2x 30 min in PTx.2 and incubated with primary antibody in PTwH and 5% DMSO/3% serum [normal donkey serum (NDS)] at 37°C for 10 days: 1:500 goat polyclonal anti-mCherry (SciGen, Ab0040). Thereafter, the brains were washed in PTwH for 10, 15, and 20 min, then every hour during the day, and then incubated at 37°C with donkey Cy5 secondary antibody 1:500 in PTwH/3% NDS for the next 10 days. Following this, they were washed in PTwH for 10, 15, and 20 min, then every hour during the day, and left overnight. Then, they were dehydrated to 20, 40, 60, 80, and then 100% methanol, 1 hour for each step, followed by 100% methanol overnight. The next day, they were put in DCM-methanol (6:4) on a shaker overnight and, the day after they were incubated, in 100% DCM 15 min twice and then changed to dibenzyl ether (DBE) for clearing. All solutions were filtered before use, and 0.02% NaN_3 was added to all stock solutions to prevent microbial growth.

The cleared hemispheres were then imaged on an Ultra Microscope II (LaVision Biotec) equipped with an sCMOS camera (Andor Neo, model 5.5-CL3) and 4x or 12x objective lenses (LaVision LVMI-Fluor 4x/0.3 or 12x/0.53 MI Plan). Two laser configurations with emission filters (525/50 for endogenous background and Alexa Fluor 488 and 680/30 for Alexa Fluor 647) were used. Image stacks were acquired with ImspectorPro64 (LaVision Biotec) using 5-μm *z*-steps. All samples were imaged in a chamber filled with DBE. Several stacks (mosaic acquisition) were taken with 10% overlap to cover each hemisphere, and the stacks were stitched to visualize the brain in 3D with Arivis Vision 4D 3.01 (Arivis AG). The movies were then compiled in Final Cut Pro 10.4.3 (Apple Inc.).

Whole-cell patch-clamp recordings in acute brain slices

Animals were decapitated under anesthesia with isoflurane (Baxter, Germany). The brain was quickly removed from the skull and placed in an ice-cold oxygenated (carbogen, 5% CO_2, and 95% O_2) *N*-methyl-D-glucamine (NMDG)–Hepes artificial cerebrospinal fluid (aCSF) containing the following: 92 mM NMDG, 2.5 mM KCl, 1.25 mM NaH_2PO_4, 30 mM $NaHCO_3$, 20 mM Hepes, 25 mM glucose, 2 mM thiourea, 5 mM Na-ascorbate, 3 mM Na-pyruvate, 0.5 mM $CaCl_2{\cdot}2H_2O$, and 10 mM $MgSO_4{\cdot}7H_2O$. We titrated the pH to 7.3 to 7.4 with 7 ± 0.2 ml of 37% hydrochloric acid, osmolarity ranging from 300 to 305 mosmol/kg. Acute brain slices containing the dorsolateral striatum were prepared at 275-μm thickness using a vibratome (Leica VT1200 S, Wetzlar, Germany). Slices were incubated for 25 min at 35°C and then transferred at RT into a holding chamber. The recordings were carried out with continuous perfusion of aCSF (1 ml/min) containing the following: 119 mM NaCl, 2.5 mM KCl, 1.3 mM $MgSO_4$, 2.5 mM $CaCl_2$, 25 mM glucose, and 26 mM $NaHCO_3$, and gassed with 95% O_2–5% CO_2 at RT (pH ~7.4, 305 mosmol/kg). The cells were visualized using a fixed-stage Olympus Microscope (BX51WI) coupled with an IR-CCD camera and a 40X water immersion objective. Patch pipettes (4- to 6-megohm resistance) were pulled from standard borosilicate glass (BF150-86-10, outer diameter: 1.5 mm, inside diameter: 0.86 mm, with filament, Sutter Instrument, Novato, CA, USA) by using a micropipette puller (p1000, Sutter Instrument, Novato, CA, USA). Recording pipettes were filled with an intracellular solution containing the following: 130 mM (K) Gluconate, 10 mM KCl, 0.2 mM EGTA, 10 mM Hepes, 4 mM (Mg) ATP, 0.5 mM (Na)GTP, and 10 mM (Na)Phosphocreatine (pH 7.25, 296 mosmol). Whole-cell patch-clamp recordings were obtained using a Multiclamp 700B amplifier and pClamp 10.4 data acquisition software (Axon Instruments, Molecular Devices, USA). The access resistance was monitored throughout the recording, and cells were discarded if the access resistance was over 35 megohms. The resting membrane potential was measured right after breaking into the cell. The capacitance of the cell was directly obtained from pClamp 10.4 data acquisition software. The input resistance (R_i) was calculated in the current clamp from a 20-pA hyperpolarizing current injection for 500 ms. AP threshold, peak amplitude AHP, and half width were

measured from the first observed spike evoked by the rheobase current injection step. Voltage responses to current injection from −20 to +35 pA with a delta of 5 pA for 500 ms were recorded at a holding potential of −70 mV. Activation of voltage-dependent sodium and potassium channels was carried out using increasing depolarizing voltage steps from −70 to +40 mV with a delta of 10 mV for 100 ms. Sodium channels were selectively blocked using 1 μM TTX (Tocris, Bristol, UK) by adding to the extracellular solution in some recordings. Data were analyzed offline using Clampfit 10.3 (Axon Instruments, Molecular Devices, USA) and Igor Pro 8.04 (Wavemetrics, Portland, OA, USA) combined with the NeuroMatic package.

Supplementary Materials

The PDF file includes:
Figs. S1 to S8
Tables S1 and S2
Legend for movie S1

Other Supplementary Material for this manuscript includes the following:
Movie S1

REFERENCES AND NOTES

1. T. Vierbuchen, A. Ostermeier, Z. P. Pang, Y. Kokubu, T. C. Südhof, M. Wernig, Direct conversion of fibroblasts to functional neurons by defined factors. *Nature* **463**, 1035–1041 (2010).
2. A. S. Yoo, A. X. Sun, L. Li, A. Shcheglovitov, T. Portmann, Y. Li, C. Lee-Messer, R. E. Dolmetsch, R. W. Tsien, G. R. Crabtree, MicroRNA-mediated conversion of human fibroblasts to neurons. *Nature* **476**, 228–231 (2011).
3. E. Y. Son, J. K. Ichida, B. J. Wainger, J. S. Toma, V. F. Rafuse, C. J. Woolf, K. Eggan, Conversion of mouse and human fibroblasts into functional spinal motor neurons. *Cell Stem Cell* **9**, 205–218 (2011).
4. M. Caiazzo, M. T. Dell'Anno, E. Dvoretskova, D. Lazarevic, S. Taverna, D. Leo, T. D. Sotnikova, A. Menegon, P. Roncaglia, G. Colciago, G. Russo, P. Carninci, G. Pezzoli, R. R. Gainetdinov, S. Gustincich, A. Dityatev, V. Broccoli, Direct generation of functional dopaminergic neurons from mouse and human fibroblasts. *Nature* **476**, 224–227 (2011).
5. U. Pfisterer, A. Kirkeby, O. Torper, J. Wood, J. Nelander, A. Dufour, A. Björklund, O. Lindvall, J. Jakobsson, M. Parmar, Direct conversion of human fibroblasts to dopaminergic neurons. *Proc. Natl. Acad. Sci. U.S.A.* **108**, 10343–10348 (2011).
6. M.-L. Liu, T. Zang, Y. Zou, J. C. Chang, J. R. Gibson, K. M. Huber, C. L. Zhang, Small molecules enable neurogenin 2 to efficiently convert human fibroblasts into cholinergic neurons. *Nat. Commun.* **4**, 2183 (2013).
7. M. Richner, M. B. Victor, Y. Liu, D. Abernathy, A. S. Yoo, MicroRNA-based conversion of human fibroblasts into striatal medium spiny neurons. *Nat. Protoc.* **10**, 1543–1555 (2015).
8. G. Colasante, G. Lignani, A. Rubio, L. Medrihan, L. Yekhlef, A. Sessa, L. Massimino, S. G. Giannelli, S. Sacchetti, M. Caiazzo, D. Leo, D. Alexopoulou, M. T. Dell'Anno, E. Ciabatti, M. Orlando, M. Studer, A. Dahl, R. R. Gainetdinov, S. Taverna, F. Benfenati, V. Broccoli, Rapid conversion of fibroblasts into functional forebrain GABAergic interneurons by direct genetic reprogramming. *Cell Stem Cell* **17**, 719–734 (2015).
9. A. Bruzelius, S. Kidnapillai, J. Drouin-Ouellet, T. Stoker, R. A. Barker, D. Rylander Ottosson, Reprogramming human adult fibroblasts into GABAergic interneurons. *Cells* **10**, 3450 (2021).
10. H. Wang, Y. Yang, J. Liu, L. Qian, Direct cell reprogramming: Approaches, mechanisms and progress. *Nat. Rev. Mol. Cell Biol.* **22**, 410–424 (2021).
11. C. J. Huh, B. Zhang, M. B. Victor, S. Dahiya, L. F. Batista, S. Horvath, A. S. Yoo, Maintenance of age in human neurons generated by microRNA-based neuronal conversion of fibroblasts. *Elife* **5**, e18648 (2016).
12. J. Mertens, J. R. Herdy, L. Traxler, S. T. Schafer, J. C. M. Schlachetzki, L. Böhnke, D. A. Reid, H. Lee, D. Zangwill, D. P. Fernandes, R. K. Agarwal, R. Lucciola, L. Zhou-Yang, L. Karbacher, F. Edenhofer, S. Stern, S. Horvath, A. C. M. Paquola, C. K. Glass, S. H. Yuan, M. Ku, A. Szücs, L. S. B. Goldstein, D. Galasko, F. H. Gage, Age-dependent instability of mature neuronal fate in induced neurons from Alzheimer's patients. *Cell Stem Cell* **28**, 1533–1548.e6 (2021).
13. K. Pircs, J. Drouin-Ouellet, V. Horváth, J. Gil, M. Rezeli, R. Garza, D. A. Grassi, Y. Sharma, I. St-Amour, K. Harris, M. E. Jönsson, P. A. Johansson, R. Vuono, S. V. Fazal, T. Stoker, B. A. Hersbach, K. Sharma, J. Lagerwall, S. Lagerström, P. Storm, S. S. Hébert, G. Marko-Varga, M. Parmar, R. A. Barker, J. Jakobsson, Distinct subcellular autophagy impairments in induced neurons from patients with Huntington's disease. *Brain* **145**, 3035–3057 (2022).
14. J. Drouin-Ouellet, E. M. Legault, F. Nilsson, K. Pircs, J. Bouquety, F. Petit, S. Shrigley, M. Birtele, M. Pereira, P. Storm, Y. Sharma, A. Bruzelius, R. Vuono, M. Kele, T. B. Stoker, D. R. Ottosson, A. Falk, J. Jakobsson, R. A. Barker, M. Parmar, Age-related pathological impairments in directly reprogrammed dopaminergic neurons derived from patients with idiopathic Parkinson's disease. *Stem Cell Reports* **17**, 2203–2219 (2022).
15. M. B. Victor, M. Richner, H. E. Olsen, S. W. Lee, A. M. Monteys, C. Ma, C. J. Huh, B. Zhang, B. L. Davidson, X. W. Yang, A. S. Yoo, Striatal neurons directly converted from Huntington's disease patient fibroblasts recapitulate age-associated disease phenotypes. *Nat. Neurosci.* **21**, 341–352 (2018).
16. Y. Xue, K. Ouyang, J. Huang, Y. Zhou, H. Ouyang, H. Li, G. Wang, Q. Wu, C. Wei, Y. Bi, L. Jiang, Z. Cai, H. Sun, K. Zhang, Y. Zhang, J. Chen, X.-D. Fu, Direct conversion of fibroblasts to neurons by reprogramming PTB-regulated microRNA circuits. *Cell* **152**, 82–96 (2013).
17. Y. Xue, H. Qian, J. Hu, B. Zhou, Y. Zhou, X. Hu, A. Karakhanyan, Z. Pang, X.-D. Fu, Sequential regulatory loops as key gatekeepers for neuronal reprogramming in human cells. *Nat. Neurosci.* **19**, 807–815 (2016).
18. X. Liu, F. Li, E. A. Stubblefield, B. Blanchard, T. L. Richards, G. A. Larson, Y. He, Q. Huang, A.-C. Tan, D. Zhang, T. A. Benke, J. R. Sladek, N. R. Zahniser, C.-Y. Li, Direct reprogramming of human fibroblasts into dopaminergic neuron-like cells. *Cell Res.* **22**, 321–332 (2012).
19. Y. Yang, R. Chen, X. Wu, Y. Zhao, Y. Fan, Z. Xiao, J. Han, L. Sun, X. Wang, J. Dai, Rapid and efficient conversion of human fibroblasts into functional neurons by small molecules. *Stem Cell Reports* **13**, 862–876 (2019).
20. J. Drouin-Ouellet, S. Lau, P. L. Brattås, D. Rylander Ottosson, K. Pircs, D. A. Grassi, L. M. Collins, R. Vuono, A. Andersson Sjöland, G. Westergren-Thorsson, C. Graff, L. Minthon, H. Toresson, R. A. Barker, J. Jakobsson, M. Parmar, REST suppression mediates neural conversion of adult human fibroblasts via microRNA-dependent and -independent pathways. *EMBO Mol. Med.* **9**, 1117–1131 (2017).
21. N. S. Rossen, P. N. Anandakumaran, R. Z. Nieden, K. Lo, W. Luo, C. Park, C. Huyan, Q. Fu, Z. Song, R. P. Singh-Moon, J. Chung, J. E. Goldenberg, N. Sampat, T. Harimoto, D. R. Bajakian, B. M. Gillette, S. K. Sia, Injectable therapeutic organoids using sacrificial hydrogels. *iScience* **23**, 101052 (2020).
22. Y. Jin, J. S. Lee, J. Kim, S. Min, S. Wi, J. H. Yu, G.-E. Chang, A.-N. Cho, Y. Choi, D.-H. Ahn, S.-R. Cho, E. Cheong, Y.-G. Kim, H.-P. Kim, Y. Kim, D. S. Kim, H. W. Kim, Z. Quan, H.-C. Kang, S.-W. Cho, Three-dimensional brain-like microenvironments facilitate the direct reprogramming of fibroblasts into therapeutic neurons. *Nat. Biomed. Eng.* **2**, 522–539 (2018).
23. A. Kirkeby, J. Nelander, D. B. Hoban, N. Rogelius, H. Bjartmarz, Novo Nordisk Cell Therapy R&D, P. Storm, A. Fiorenzano, A. F. Adler, S. Vale, J. Mudannayake, Y. Zhang, T. Cardoso, B. Mattsson, A. M. Landau, A. N. Glud, J. C. Sorensen, T. P. Lillethorup, M. Lowdell, C. Carvalho, O. Bain, T. van Vliet, O. Lindvall, A. Bjorklund, B. Harry, E. Cutting, H. Widner, G. Paul, R. A. Barker, M. Parmar, Preclinical quality, safety, and efficacy of a human embryonic stem cell-derived product for the treatment of Parkinson's disease, STEM-PD. *Cell Stem Cell* **30**, 1299–1314.e9 (2023).
24. J. Drouin-Ouellet, M. Parmar, R. A. Barker, K. Pircs, S. Shrigley, Simple generation of a high yield culture of induced neurons from human adult skin fibroblasts. *J. Vis. Exp.* **5**, 56904 (2018).
25. S. Horvath, DNA methylation age of human tissues and cell types. *Genome Biol.* **14**, R115 (2013).
26. B. Roy, L. Yuan, Y. Lee, A. Bharti, A. Mitra, G. V. Shivashankar, Fibroblast rejuvenation by mechanical reprogramming and redifferentiation. *Proc. Natl. Acad. Sci. U.S.A.* **117**, 10131–10141 (2020).
27. A. Conesa, M. J. Nueda, A. Ferrer, M. Talon, maSigPro: A method to identify significantly differential expression profiles in time-course microarray experiments. *Bioinformatics* **22**, 1096–1102 (2006).
28. A. Fiorenzano, P. Storm, E. Sozzi, A. Bruzelius, S. Corsi, J. Kajtez, J. Mudannayake, J. Nelander, B. Mattsson, M. Åkerblom, T. Bjorklund, A. Björklund, M. Parmar, TARGET-seq: Linking single-cell transcriptomics of human dopaminergic neurons with their target specificity. *Proc. Natl. Acad. Sci. U.S.A.* **121**, e2410331121 (2024).
29. H. Wang, B. Keepers, Y. Qian, Y. Xie, M. Colon, J. Liu, L. Qian, Cross-lineage potential of Ascl1 uncovered by comparing diverse reprogramming regulatomes. *Cell Stem Cell* **29**, 1491–1504.e9 (2022).
30. B. Treutlein, Q. Y. Lee, J. G. Camp, M. Mall, W. Koh, S. A. Shariati, S. Sim, N. F. Neff, J. M. Skotheim, M. Wernig, S. R. Quake, Dissecting direct reprogramming from fibroblast to neuron using single-cell RNA-seq. *Nature* **534**, 391–395 (2016).
31. H. Bading, D. D. Ginty, M. E. Greenberg, Regulation of gene expression in hippocampal neurons by distinct calcium signaling pathways. *Science* **260**, 181–186 (1993).
32. F. Sun, J. Zeng, M. Jing, J. Zhou, J. Feng, S. F. Owen, Y. Luo, F. Li, H. Wang, T. Yamaguchi, Z. Yong, Y. Gao, W. Peng, L. Wang, S. Zhang, J. Du, D. Lin, M. Xu, A. C. Kreitzer, G. Cui, Y. Li, A genetically encoded fluorescent sensor enables rapid and specific detection of dopamine in flies, fish, and mice. *Cell* **174**, 481–496.e19 (2018).

33. C. Klein Herenbrink, J. F. Støier, W. D. Reith, A. Dagra, M. A. C. Gregorek, R. B. Cola, T. Patriarchi, Y. Li, L. Tian, U. Gether, F. Herborg, Multimodal detection of dopamine by sniffer cells expressing genetically encoded fluorescent sensors. *Commun. Biol.* **5**, 578 (2022).
34. J. A. Bagley, D. Reumann, S. Bian, J. Lévi-Strauss, J. A. Knoblich, Fused cerebral organoids model interactions between brain regions. *Nat. Methods* **14**, 743–751 (2017).
35. C. Martins-Costa, A. Wiegers, V. A. Pham, J. Sidhaye, B. Doleschall, M. Novatchkova, T. Lendl, M. Piber, A. Peer, P. Möseneder, M. Stuempflen, S. Y. A. Chow, R. Seidl, D. Prayer, R. Höftberger, G. Kasprian, Y. Ikeuchi, N. S. Corsini, J. A. Knoblich, ARID1B controls transcriptional programs of axon projection in an organoid model of the human corpus callosum. *Cell Stem Cell* **31**, 866–885.e14 (2024).
36. K. Miyamichi, F. Amat, F. Moussavi, C. Wang, I. Wickersham, N. R. Wall, H. Taniguchi, B. Tasic, Z. J. Huang, Z. He, E. M. Callaway, M. A. Horowitz, L. Luo, Cortical representations of olfactory input by trans-synaptic tracing. *Nature* **472**, 191–196 (2011).
37. S. Grealish, A. Heuer, T. Cardoso, A. Kirkeby, M. Jönsson, J. Johansson, A. Björklund, J. Jakobsson, M. Parmar, Monosynaptic tracing using modified rabies virus reveals early and extensive circuit integration of human embryonic stem cell-derived neurons. *Stem Cell Reports* **4**, 975–983 (2015).
38. S. Nolbrant, A. Heuer, M. Parmar, A. Kirkeby, Generation of high-purity human ventral midbrain dopaminergic progenitors for in vitro maturation and intracerebral transplantation. *Nat. Protoc.* **12**, 1962–1979 (2017).
39. J. R. Clay, D. B. Forger, D. Paydarfar, Ionic mechanism underlying optimal stimuli for neuronal excitation: Role of Na^+ channel inactivation. *PLOS ONE* **7**, e45983 (2012).
40. J. Kajtez, F. Nilsson, A. Fiorenzano, M. Parmar, J. Emnéus, 3D biomaterial models of human brain disease. *Neurochem. Int.* **147**, 105043 (2021).
41. S. Velasco, B. Paulsen, P. Arlotta, 3D brain organoids: Studying brain development and disease outside the embryo. *Annu. Rev. Neurosci.* **43**, 375–389 (2020).
42. R. Bocchi, G. Masserdotti, M. Götz, Direct neuronal reprogramming: Fast forward from new concepts toward therapeutic approaches. *Neuron* **110**, 366–393 (2022).
43. L. Pasitka, M. Cohen, A. Ehrlich, B. Gildor, E. Reuveni, M. Ayyash, G. Wissotsky, A. Herscovici, R. Kaminker, A. Niv, R. Bitcover, O. Dadia, A. Rudik, A. Voloschin, M. Shimoni, Y. Cinnamon, Y. Nahmias, Spontaneous immortalization of chicken fibroblasts generates stable, high-yield cell lines for serum-free production of cultured meat. *Nat. Food* **4**, 35–50 (2023).
44. Z. Xu, Y. Li, P. Li, Y. Sun, S. Lv, Y. Wang, X. He, J. Xu, Z. Xu, L. Li, Y. Li, Soft substrates promote direct chemical reprogramming of fibroblasts into neurons. *Acta Biomater.* **152**, 255–272 (2022).
45. Z. Sun, J.-S. Kwon, Y. Ren, S. Chen, C. K. Walker, X. Lu, K. Cates, H. Karahan, S. Sviben, J. A. J. Fitzpatrick, C. Valdez, H. Houlden, C. M. Karch, R. J. Bateman, C. Sato, S. J. Mennerick, M. I. Diamond, J. Kim, R. E. Tanzi, D. M. Holtzman, A. S. Yoo, Modeling late-onset Alzheimer's disease neuropathology via direct neuronal reprogramming. *Science* **385**, adl2992 (2024).
46. J. Mertens, A. C. M. Paquola, M. Ku, E. Hatch, L. Böhnke, S. Ladjevardi, S. McGrath, B. Campbell, H. Lee, J. R. Herdy, J. T. Gonçalves, T. Toda, Y. Kim, J. Winkler, J. Yao, M. W. Hetzer, F. H. Gage, Directly reprogrammed human neurons retain aging-associated transcriptomic signatures and reveal age-related nucleocytoplasmic defects. *Cell Stem Cell* **17**, 705–718 (2015).
47. Y. Miura, M.-Y. Li, F. Birey, K. Ikeda, O. Revah, M. V. Thete, J.-Y. Park, A. Puno, S. H. Lee, M. H. Porteus, S. P. Paşca, Generation of human striatal organoids and cortico-striatal assembloids from human pluripotent stem cells. *Nat. Biotechnol.* **38**, 1421–1430 (2020).
48. J. Giacomoni, A. Bruzelius, M. Habekost, J. Kajtez, D. R. Ottosson, A. Fiorenzano, P. Storm, M. Parmar, 3D model for human glia conversion into subtype-specific neurons, including dopamine neurons. *Cell Rep. Methods* **4**, 100845 (2024).
49. F. Oltolina, A. Zamperone, D. Colangelo, L. Gregoletto, S. Reano, S. Pietronave, S. Merlin, M. Talmon, E. Novelli, M. Diena, C. Nicoletti, A. Musarò, N. Filigheddu, A. Follenzi, M. Prat, Human cardiac progenitor spheroids exhibit enhanced engraftment potential. *PLOS ONE* **10**, e0137999 (2015).
50. S. Uchida, K. Itaka, T. Nomoto, T. Endo, Y. Matsumoto, T. Ishii, K. Kataoka, An injectable spheroid system with genetic modification for cell transplantation therapy. *Biomaterials* **35**, 2499–2506 (2014).
51. M. B. Victor, M. Richner, T. O. Hermanstyne, J. L. Ransdell, C. Sobieski, P.-Y. Deng, V. A. Klyachko, J. M. Nerbonne, A. S. Yoo, Generation of human striatal neurons by microRNA-dependent direct conversion of fibroblasts. *Neuron* **84**, 311–323 (2014).
52. D. G. Abernathy, W. K. Kim, M. J. McCoy, A. M. Lake, R. Ouwenga, S. W. Lee, X. Xing, D. Li, H. J. Lee, R. O. Heuckeroth, J. D. Dougherty, T. Wang, A. S. Yoo, MicroRNAs induce a permissive chromatin environment that enables neuronal subtype-specific reprogramming of adult human fibroblasts. *Cell Stem Cell* **21**, 332–348.e9 (2017).
53. E. Quist, F. Trovato, N. Avaliani, O. G. Zetterdahl, A. Gonzalez-Ramos, M. G. Hansen, M. Kokaia, I. Canals, H. Ahlenius, Transcription factor-based direct conversion of human fibroblasts to functional astrocytes. *Stem Cell Reports* **17**, 1620–1635 (2022).
54. I. Canals, A. Ginisty, E. Quist, R. Timmerman, J. Fritze, G. Miskinyte, E. Monni, M. G. Hansen, I. Hidalgo, D. Bryder, J. Bengzon, H. Ahlenius, Rapid and efficient induction of functional astrocytes from human pluripotent stem cells. *Nat. Methods* **15**, 693–696 (2018).
55. M. Caiazzo, S. Giannelli, P. Valente, G. Lignani, A. Carissimo, A. Sessa, G. Colasante, R. Bartolomeo, L. Massimino, S. Ferroni, C. Settembre, F. Benfenati, V. Broccoli, Direct conversion of fibroblasts into functional astrocytes by defined transcription factors. *Stem Cell Reports* **4**, 25–36 (2015).
56. K. Chanoumidou, B. Hernández-Rodríguez, F. Windener, C. Thomas, M. Stehling, S. Mozafari, S. Albrecht, L. Ottoboni, J. Antel, K.-P. Kim, S. Velychko, Q. L. Cui, Y. K. T. Xu, G. Martino, J. Winkler, H. R. Schöler, A. B.-V. Evercooren, O. Boespflug-Tanguy, J. M. Vaquerizas, M. Ehrlich, T. Kuhlmann, One-step reprogramming of human fibroblasts into oligodendrocyte-like cells by SOX10, OLIG2, and NKX6.2. *Stem Cell Reports* **16**, 771–783 (2021).
57. K. Tanabe, H. Nobuta, N. Yang, C. E. Ang, P. Huie, S. Jordan, M. C. Oldham, D. H. Rowitch, M. Wernig, Generation of functional human oligodendrocytes from dermal fibroblasts by direct lineage conversion. *Development* **149**, dev199723 (2022).
58. R. Zufferey, D. Nagy, R. J. Mandel, L. Naldini, D. Trono, Multiply attenuated lentiviral vector achieves efficient gene delivery in vivo. *Nat. Biotechnol.* **15**, 871–875 (1997).
59. J. S. Rothman, R. A. Silver, NeuroMatic: An integrated open-source software toolkit for acquisition, analysis and simulation of electrophysiological data. *Front. Neuroinform.* **12**, 14 (2018).
60. A. Dobin, C. A. Davis, F. Schlesinger, J. Drenkow, C. Zaleski, S. Jha, P. Batut, M. Chaisson, T. R. Gingeras, STAR: Ultrafast universal RNA-seq aligner. *Bioinformatics* **29**, 15–21 (2013).
61. R. Patro, G. Duggal, M. I. Love, R. A. Irizarry, C. Kingsford, Salmon provides fast and bias-aware quantification of transcript expression. *Nat. Methods* **14**, 417–419 (2017).
62. M. I. Love, W. Huber, S. Anders, Moderated estimation of fold change and dispersion for RNA-seq data with DESeq2. *Genome Biol.* **15**, 550 (2014).
63. M. D. Young, M. J. Wakefield, G. K. Smyth, A. Oshlack, Gene ontology analysis for RNA-seq: Accounting for selection bias. *Genome Biol.* **11**, R14 (2010).
64. F. Supek, M. Bosnjak, N. Skunca, T. Smuc, REVIGO summarizes and visualizes long lists of gene ontology terms. *PLOS ONE* **6**, e21800 (2011).
65. X. Ren, P. F. Kuan, RNAAgeCalc: A multi-tissue transcriptional age calculator. *PLOS ONE* **15**, e0237006 (2020).
66. M. J. Aryee, A. E. Jaffe, H. Corrada-Bravo, C. Ladd-Acosta, A. P. Feinberg, K. D. Hansen, R. A. Irizarry, Minfi: A flexible and comprehensive Bioconductor package for the analysis of Infinium DNA methylation microarrays. *Bioinformatics* **30**, 1363–1369 (2014).
67. N. Renier, Z. Wu, D. J. Simon, J. Yang, P. Ariel, M. Tessier-Lavigne, iDISCO: A simple, rapid method to immunolabel large tissue samples for volume imaging. *Cell* **159**, 896–910 (2014).
68. R. Edgar, M. Domrachev, A. E. Lash, Gene Expression Omnibus: NCBI gene expression and hybridization array data repository. *Nucleic Acids Res.* **30**, 207–210 (2002).

Acknowledgments: We would like to thank M. Sparrenius for the help with animal work; U. Jarl and B. Mattsson for providing help with sample preparation, imaging, and image reconstruction for iDISCO of the whole rat brains; S. da Rocha Baez for the help with virus production; E. Sozzi and J. Johansson for technical assistance with sequencing preparation; N. Avaliani from the Electrophysiology core facility at Lund Stem Cell Center for the help with ex vivo electrophysiological measurements; and A. Athanasiou-Fragkouli for sharing the AST fibroblast line. Lund University Bioimaging Centre (LBIC) is gratefully acknowledged for providing experimental resources for confocal microscopy. Methylation profiling was performed by the SNP&SEQ Technology Platform in Uppsala (www.genotyping.se). The facility is part of the National Genomics Infrastructure supported by the Swedish Research Council for Infrastructures and Science for Life Laboratory, Sweden. **Funding:** This work was supported by funding from the New York Stem Cell Foundation (M.P.), European Research Council (ERC) under ERC Grant Agreement 771427 (M.P.), European Union–funded project NSC-Reconstruct [European Union, H2020, GA no. 874758, 2020-23 (M.P.)], Swedish Research Council [2021-00661 (M.P.),2021-02967 (M.P.), and 2021-01839 (D.R.O.)], Swedish Parkinson Foundation [Parkinsonfonden (M.P.)], Swedish Brain Foundation (M.P.), Konung Gustaf V:s och Drottning Victorias Frimurarestiftelse (M.P.), Olle Engkvist Foundation [213-0229 (D.R.O.), Anna-Lisa Rosenberg Foundation (E.C.-P.), Royal Physiographic Society in Lund [43202 (E.C.-P.)], Strategic Research Area at Lund University Multipark (M.P.), Lundbeck Foundation Postdoc Fellowship [R347-2020-2522 (M.H.)], and Segerfalk Foundation (J.K.). **Author contributions:** Conceptualization: J.K., K.L., F.N., A.B., M.B., A.F., M.H., and M.P. Data curation: P.S. Formal analysis: J.K., K.L., A.B., P.S., A.F., and M.H. Funding acquisition: M.P. and D.R.O. Investigation: J.K., K.L., F.N., A.B., E.C.-P., M.B., and A.F. Methodology: J.K., K.L., F.N., M.P., A.F., D.R.O., A.B., F.H., and R.A.B. Resources: R.A.B., F.H., D.R.O., and F.N. Project administration: J.K. and M.P. Software: P.S. Supervision: M.P. Validation: J.K., K.L., F.N., P.S., and M.P. Visualization: J.K., K.L., M.P., A.B., and E.C.-P. Writing—original draft: J.K. and M.P. Writing—review and editing: K.L., M.H., P.S., A.B., F.N., E.C.-P., D.R.O., R.A.B., and F.H. **Competing interests:** M.P. is the owner of Parmar Cells AB

and coinventor of the following patents: WO2016162747A2, WO2018206798A1, and WO2019016113A1. M.P. performs paid consultancy and commissioned research for Novo Nordisk AS Cell Therapy Research and Development unit and serves on the SAB for Arbor Bio. The other authors declare that they have no competing interests. **Data and materials availability:** All data needed to evaluate the conclusions in the paper are present in the paper and/or the Supplementary Materials. The data discussed in this publication have been deposited in NCBI's Gene Expression Omnibus (*68*) and are accessible through GEO Series accession number GSE287155 at the following link: https://ncbi.nlm.nih.gov/geo/query/acc.cgi?acc=GSE287155.

Submitted 30 May 2024
Accepted 1 May 2025
Published 6 June 2025
10.1126/sciadv.adq7855